Forschungszentrum Karlsruhe
in der Helmholtz-Gemeinschaft

Wissenschaftliche Berichte
FZKA 7292

Investigations of the Muon Component of Extensive Air Showers Measured by KASCADE-Grande

J. van Buren

Institut für Kernphysik

März 2007

Forschungszentrum Karlsruhe

in der Helmholtz-Gemeinschaft

Wissenschaftliche Berichte

FZKA 7292

Investigations of the Muon Component of Extensive Air Showers Measured by KASCADE-Grande

Jurriaan van Buren

Institut für Kernphysik

Von der Fakultät für Physik der Universität Karlsruhe (TH)
genehmigte Dissertation

Forschungszentrum Karlsruhe GmbH, Karlsruhe

2007

Forschungszentrum Karlsruhe GmbH
Postfach 3640, 76021 Karlsruhe

Mitglied der Hermann von Helmholtz-Gemeinschaft
Deutscher Forschungszentren (HGF)

ISSN 0947-8620

urn:nbn:de:0005-072922

Abstract

The energy spectrum of cosmic rays shows a change of the spectral behavior at an energy of about $4 \cdot 10^{15}$ eV, the so-called knee. Results of the KASCADE experiment show that it is caused by a change of flux in the light component of cosmic rays. With the extension to the KASCADE-Grande experiment it is possible to measure air showers up to an energy of 10^{18} eV, covering the range where one expects the knee in the heavy component, the so-called second knee. In order to estimate the number of muons of an air shower measured by KASCADE-Grande, the muon detectors of KASCADE array are used, allowing the measurement of the muon component in a distance of 40 m to 700 m to the shower core over a radial range of up to 280 m. It is shown that the reconstruction is possible and unfolding methods are applied to obtain the total energy spectra of cosmic rays from the measured muon size spectra for the zenith angle ranges 0°–18° and 18°–25°. These unfolding procedures base on simulations of air showers using the interaction models FLUKA and QGSJet. A comparison with previous results of KASCADE for zenith angles 0°–18° shows a good agreement in the overlap range 10^{16} eV to 10^{17} eV. The energy spectra extend up to an energy of $3 \cdot 10^{17}$ eV and show with the available statistics so far no second knee.

Zusammenfassung

Untersuchung der myonischen Komponente ausgedehnter Luftschauer mit dem KASCADE-Grande Experiment

Das Energiespektrum der kosmischen Strahlung zeigt bei einer Energie von etwa $4 \cdot 10^{15}$ eV ein Steilerwerden des Spektrums, das sogenannte Knie. Ergebnisse von KASCADE zeigen, dass es durch eine Abnahme des Flusses in der leichten Komponente hervorgerufen wird. Mit der Erweiterung zum KASCADE-Grande Experiment ist es möglich, ausgedehnte Luftschauer bis zu einer Energie von 10^{18} eV zu messen und so das erwartete schwere, bzw. zweite Knie nachzuweisen. Um in KASCADE-Grande die Myonzahl eines Luftschauers zu bestimmen, verwendet man die Myondetektoren des KASCADE Detektorfeldes. Dies erlaubt die Messung der Myonkomponente in einem Abstand von 40 m bis 700 m über einen radialen Bereich von bis zu 280 m. Es wird gezeigt, daß die Rekonstruktion möglich ist und es werden mit Entfaltungsmethoden aus den Myongrößenspektren die Energiespektren für die Zenitwinkelbereiche 0°–18° und 18°–25° bestimmt. Diese Entfaltungsmethoden basieren auf Simulationen mit den Wechselwirkungsmodellen FLUKA und QGSJet. Ein Vergleich mit bisherigen Ergebnissen von KASCADE im Zenitwinkelbereich 0°–18° zeigt eine gute Übereinstimmung im Überlappbereich 10^{16} eV bis 10^{17} eV. Die Energiespektren erstrecken sich bis zu einer Energie von $3 \cdot 10^{17}$ eV und zeigen mit der bisher zur Verfügung stehenden Statistik kein zweites Knie.

Contents

Chapter 1

Introduction

The flux of the cosmic rays can be described by a power law $dN/dE \propto E^{-\gamma}$, where γ is the spectral index. The all-particle energy spectrum of cosmic rays shows a distinctive discontinuity at few PeV, known as the *knee*, where the spectral index changes from 2.7 to approximately 3.1. This discontinuity is caused by a superposition of knees in the lighter components of cosmic rays [11]. There exist various theories trying to explain the knee, some predict knee positions occurring at constant rigidity of the particles. On the other hand, the hypothesis of new hadronic interaction mechanisms at the knee energy implies an dependence of the knee positions on the atomic mass.
The KASCADE experiment was extended by the Grande array consisting of 37 stations spread on a collecting area of 0.5 km^2. With this setup the study of cosmic rays up to energies of 10^{18} eV is possible and allows to answer the question whether there is a second knee caused by a discontinuity in the heavy component and whether its position shows a rigidity or mass dependence. Furthermore it allows the measurement of a possible transition region from galactic to extragalactic cosmic rays, where there is no theoretical reason for a smooth crossover in slope and flux.
The purpose of the work described in this thesis is the reconstruction and analysis of the muon component of extensive air showers measured by KASCADE-Grande. The muon spectrum is an essential information to be able to determine the energy spectra of different mass groups. It is shown that with unfolding methods it is possible to obtain the total energy spectrum from the measured muon spectrum. This work presents the first experimental results obtained analyzing the KASCADE-Grande data.
In Chapter 2 an overview is given of the current knowledge and theoretical models about composition, acceleration and propagation of cosmic rays. Furthermore a summary of the characteristics of extensive air showers, especially how they differ at observation level for different primary cosmic ray particles, is given.
The experimental setup of KASCADE-Grande to measure extensive air showers is illustrated in Chapter 3, where the detector parts that measure various components of air showers are described.

Chapter 4 explains the methods applied to reconstruct air showers measured with KASCADE-Grande. It specifies the lateral energy correction function, to convert measured energy deposits to particle densities in the muon detector, and the lateral distribution function to describe the measured muon densities.
Chapter 5 discusses the measured muon component, i.e. the muon lateral distribution and the muon size spectrum.
To take account of the muon size distributions at a given energy, unfolding methods are considered in Chapter 6. These unfolding methods are applied to data and its results are presented in Chapter 7. Finally Chapter 8 draws the conclusions.

Chapter 2

Cosmic Rays

The atmosphere of the Earth is hit by a flux of cosmic ray particles, consisting of ionized nuclei, mostly protons and alpha particles, and for a small fraction of photons and electrons. They were first discovered in 1911 by Viktor F. Hess [35] on several balloon flights, where he showed that it was penetrating radiation coming from space, not from the Earth below as thought before.
Originally understood as penetrating γ-radiation, in the late twenties Compton and others realized that cosmic rays mainly consist of charged particles. In the next years it was a source for discoveries in the field of particle physics, e.g. the positron in 1933 [6] and the muon in 1937 [7], that are secondary particles produced in the interaction of the primary cosmic ray particle.
Soon it was clear that the cosmic ray particles cover large energy ranges. Pierre Auger discovered in coincidence measurements extensive air showers initiated by single cosmic ray particles [13] of an estimated energy of 10^{15} eV. The up to now highest energy cosmic ray ever measured had an energy of 3×10^{20} eV [16]. Fundamental questions that arise are "Where do they come from?" and "How are they accelerated?".
In this chapter a short overview is given of the current knowledge and theoretical models about composition, acceleration and propagation of cosmic rays.

2.1 The Energy Spectrum

The energy spectrum of the cosmic rays covers an energy range from approximately 10^{10} eV–10^{20} eV and the flux decreases by more than 30 orders of magnitude in this range. The flux can be described by a power law with a spectral index γ in the range of 2.5 – 3.2:

$$\frac{dN}{dE} \propto E^{-\gamma} \tag{2.1}$$

In Figure 2.1 an overview of measured energy spectra by several experiments is shown, with the flux multiplied by $E^{3.}$ to clarify the structures in the spectrum.

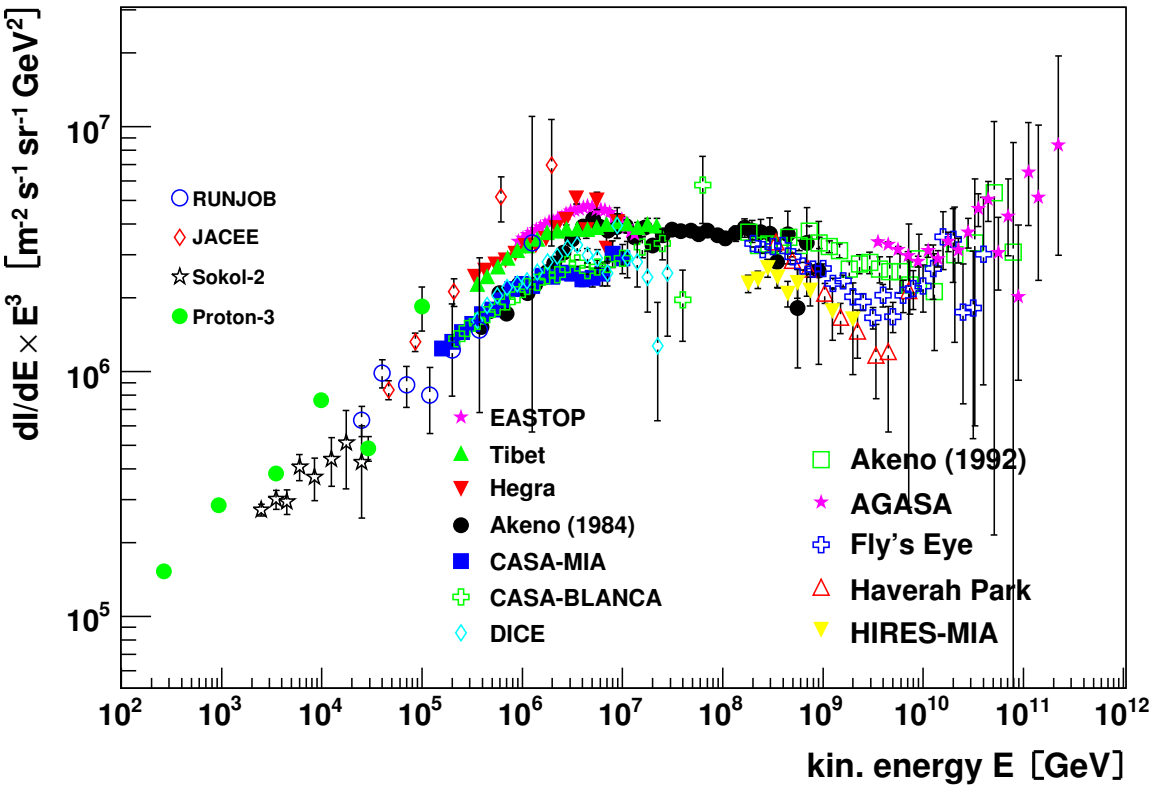

Figure 2.1: Overview of measurements of the energy spectrum of cosmic rays taken from [57]. References to experiments see within.

Particles with energies up to around 100 TeV can be measured by balloon or satellite experiments, for higher energies the flux is too low to be determined by direct measurements. At similar energies though, from 100 TeV–1000 TeV, a cosmic ray produces enough secondaries to trigger a ground array.
At an energy of around 4 PeV one sees an change of the index, the so-called knee, where the index γ changes from approximately 2.7 to 3.1. It was first observed in 1958 in an experiment at Moscow university [40].
At an energy of approximately 4×10^{17} eV some experiments report a steepening in the spectrum, which is most apparent in the Yakutsk [41], HiRes-MIA [2], and Fly's Eye stereo [15] data and is usually referred to as the "second knee". The spectral index changes from approximately 3 to 3.3 .
At an energy of around 4×10^{18} eV a flattening of the spectrum is observed, the ankle, with the spectral index becoming ≈ 2.8. This is presumably due to a take over from the galactic component to a harder extra galactic component.
At highest energies above 5×10^{19} eV data is sparse and the shape of the spectrum under discussion, whether or not the so-called GZK cutoff is observed [54, 53, 14].

At energies of approximately 5×10^{19} eV the mean free path of protons is reduced by more than two orders of magnitudes, due to pion-production on cosmic microwave background photons, the Greisen-Zatsepin-Kuzmin effect [32, 60]. Nuclei show an ever stronger cutoff at moderately higher energies.

2.2 The Composition of Cosmic Rays

Up to energies of some 100 TeV the flux of particles is sufficiently high to be accessible by high flying balloon or satellite experiments that can study elemental distributions. These measurements provide important implications for the origin and transport properties of cosmic rays in the interstellar medium.
Comparing the elemental abundances of the solar system with the cosmic rays, one sees several differences. Two groups of elements are much more abundant in cosmic rays than in our solar system, namely the group of Li, Be, B and at higher masses Sc, Ti, V, Cr, Mn. They are spallation products of heavier elements as Carbon and Oxygen for the first group and iron for the second group, produced in collisions with the interstellar medium.
For energies of few Gev per nucleon one finds the amount of matter traversed is $5 - 10$ g/cm^2 which corresponds to a path length of approximately 1000 kpc. This is much larger than the thickness of the galactic disk (1kpc), which means that the cosmic rays diffuse through the galaxy and its halo for a long time before escaping. With increasing energy to several hundreds of GeV per nucleon the relative abundance of secondaries decreases, which means that less matter is traversed and the escape time has decreased.
Because of different densities in the galactic disk and its halo, it is difficult to deduce the escape time from the average thickness of matter traversed. This is possible by analyzing the ratio of radioactive secondaries and its decay products, e.g. for ^{10}Be/^{9}Be yields 10^7 years as age of cosmic rays. For energies from approximately 1 TeV 100 TeV Hydrogen and Helium are the dominating contributions.
Above 10^{15} eV all information derives from studies of extensive air showers and their interpretation relies on model calculations.
In the range of the knee the composition changes to heavier elements [11]. Above energies of 10^{17} eV the fraction of heavy nuclei decreases to approximately 30%. At highest energies the situation is not clear. The HiRes group and Yakutsk group report a predominantly light composition, possibly slowly changing [1, 41]. The AGASA experiment instead reports a heavier composition [55].

2.3 Acceleration and Propagation

Acceleration The locally observed energy density of cosmic rays is $\epsilon \approx 1\text{eV/cm}^3$. The power required to fill the volume of the whole galaxy equals to $\approx 5 \times 10^{33}\text{J/s}$, comparing this to the power of supernovae is suggestive to see them as the sites of acceleration. In our galaxy about 3 Supernovae explosions occur per century, which yields a power of around $3 \times 10^{35}\text{J/s}$. So an efficiency of a few percent would be enough for supernova shock waves to energize the galactic cosmic rays.
The most important acceleration process is the diffusive acceleration at shock waves [27, 22]. A particle traverses a shock wave several times as on either side it scatters back in a diffuse scattering on magnetic irregularities. In this process called *Fermi acceleration* a particle gains energy proportional to the speed of the wave and the maximal achievable energy depends on the number of crossings and the time spent in the surrounding of the shock wave. It produces an energy spectrum that can be described by a power law $E^{-\gamma}$ with $\gamma \approx 2$. First hints for acceleration of hadrons at supernova remnants were measured by CANGAROO [24] and HESS[5]. These experiments measure TeV gamma rays created by collision of accelerated protons with atoms and molecules in an interstellar cloud.
Different sites of acceleration could be neighboring stars of pulsars that are hit by the pulsar wind [33], or accreting matter from neighboring stars or at the shock wave of the galactic wind [36]. Further mechanisms of acceleration are direct acceleration in strong electric or magnetic field, e.g. at polar caps of pulsars [20].
For energies above 10^{17} eV the origins are not clear. Possible candidates are e.g. jets of Active Galactic Nuclei [49]. For higher energies above 10^{19} eV there exist also various Top-down models in which the cosmic rays are produces as decay products of some super heavy particles X with mass $m_X \geq 10^{12}$ GeV. An overview on Top-down candidates is given in [52].

Propagation Cosmic rays in the energy range up to several hundred PeV have a galactic origin. Their propagation in the interstellar medium is mainly determined by their interaction with magnetic and electric fields in the cosmic plasma. Further important factors are spallation, ionization losses and radioactive decay. These processes cause a change of the index of the energy spectrum from initially $\gamma \approx 2$ to an observed value of $\gamma \approx 2.7$.
As already mentioned, from the ratio of secondaries to primaries one can conclude that the cosmic rays travel distances through the galaxy a factor thousand larger than the thickness of the galaxy. The observed ratio of boron to carbon suggests that higher energetic particles traverse less matter as they escape earlier from the galaxy. Furthermore it implies that the acceleration occurs before the propagation, else the ratio would be constant or increase with energy.

2.4 Possible Origin of the Knee in the Energy Spectrum

There are various models that offer an explanation to the change of the index from ≈ 2.7 to ≈ 3.1 at an energy of around 4 PeV. They apply at different stages of the cosmic rays, interpreting the knee as a limit or change of acceleration process, as an effect during propagating through the galaxy, and finally as an effect of observing the interactions of cosmic rays with the Earth's atmosphere. Furthermore they can be classified in astrophysical or particle physics models. In the following a short overview of the models is given and their possible observational signature.

Acceleration
In many models the "knee energy" is considered as the maximum achievable acceleration energy. As acceleration occurs at shock waves the achievable energy is proportional to the charge Z of the nuclei , the strength of the magnetic field and the characteristic time of acceleration. Maximum energies range from $Z \times 10^{13}$ eV [42] to $Z \times 10^{14}$ eV.
In the "Single Source Model" [25] the knee results from a young and relatively nearby supernova remnant, its shock wave recently propagated or currently propagates through the solar system. The particles accelerated by this close supernova remnant form an energy spectrum exhibiting a knee, the position for the single elements scaling with the charge. This energy spectrum superimposes with a featureless background spectrum created by several background sources.

Propagation
Other astrophysical models suggest that the knee originates from propagation effects of the cosmic rays through the galaxy. This requires that particles are accelerated to energies higher than the range of the knee. The diffusion coefficients depend on the energy and this causes the knee in the energy spectrum (e.g. [48], [19]). Below the knee the normal transverse diffusion dominates, above the knee the Hall diffusion which lets more particles escape from the galaxy and results in a steepening of the spectrum.
With a typical magnetic field of 3 μG and characteristic length of 1 pc, particles with a rigidity of 3×10^6 GV are contained in the galaxy, higher energetic particles will escape from it.

Exotic models
There exist various models to explain the knee in the energy spectrum based on exotic physics. That means for example that they introduce new particles or new characteristic in interaction of particles. In the following three examples are shortly described. Considering neutrinos having a mass, the inverse β reaction $p + (\bar{\nu}_e) \longrightarrow n + e^+$ could

destroy protons. In [59] it is suggested that this reaction occurs with protons of cosmic rays and relic Big Bang neutrinos and the knee energy $E_{knee} \simeq 4$ PeV corresponds to a rest mass of neutrinos $m_\nu \simeq 0.4$ eV. A second knee is expected at 3×10^{17} eV corresponding to the threshold energy for above reaction with α particles.
There are suggestions that the knee observed is not a characteristic of the spectrum itself, but due to its observation on earth. Due to changes in the high energy interactions, a new type of heavy particles might be produced in the first interaction with the Earth's atmosphere and escape unseen [46]. The extensive air shower measured on ground would appear lower energetic, thus the energy assigned to an event would lower and the resulting energy spectrum becomes steeper.
A similar explanation offers [39], the steepening at the knee due to new interactions, low scale gravity, which produce particles undetected by the experimental apparatus. The missing energy leads to an underestimate of the true energy and generates a break in the reconstructed cosmic ray spectrum.
These particle physics explanations of the knee have in common that the position of individual elements would scale with their mass number A and not their nuclear charge Z.

2.5 Extensive Air Showers

An Extensive Air Shower is initiated when a high energetic cosmic ray particle interacts with an atom of the Earth's atmosphere, typically a Nitrogen or Oxygen atom. In this first interaction occurring in a height of 10 km – 40 km the primary particle is fragmented and new hadrons are produced, mainly pions and kaons, that interact with other atoms of the atmosphere and produce further secondaries. The number of particles increases until reaching a maximum, as the average energy per particle decreases and more and more particles fall below the threshold for further particle production. The total number of particles in the air shower then decreases approximately exponentially (see Figure 2.3 left). In Figure 2.2 a schematic view of an extensive air showers is shown, with the secondary particles reaching ground in a shower disk of about 1m thickness.

An air shower consists of three components, electromagnetic, muonic and hadronic.

Hadronic Component
The core of the air shower is formed by high energetic hadrons, nuclei fragments, protons, neutrons and mesons. It has a small lateral spread of around ≈ 20 m, only low energetic hadrons, mainly neutrons, can spread further. High energetic hadrons contribute further to the hadronic cascade. The decay of neutral mesons feeds the electromagnetic component, lower energetic charged mesons feed the muonic component.

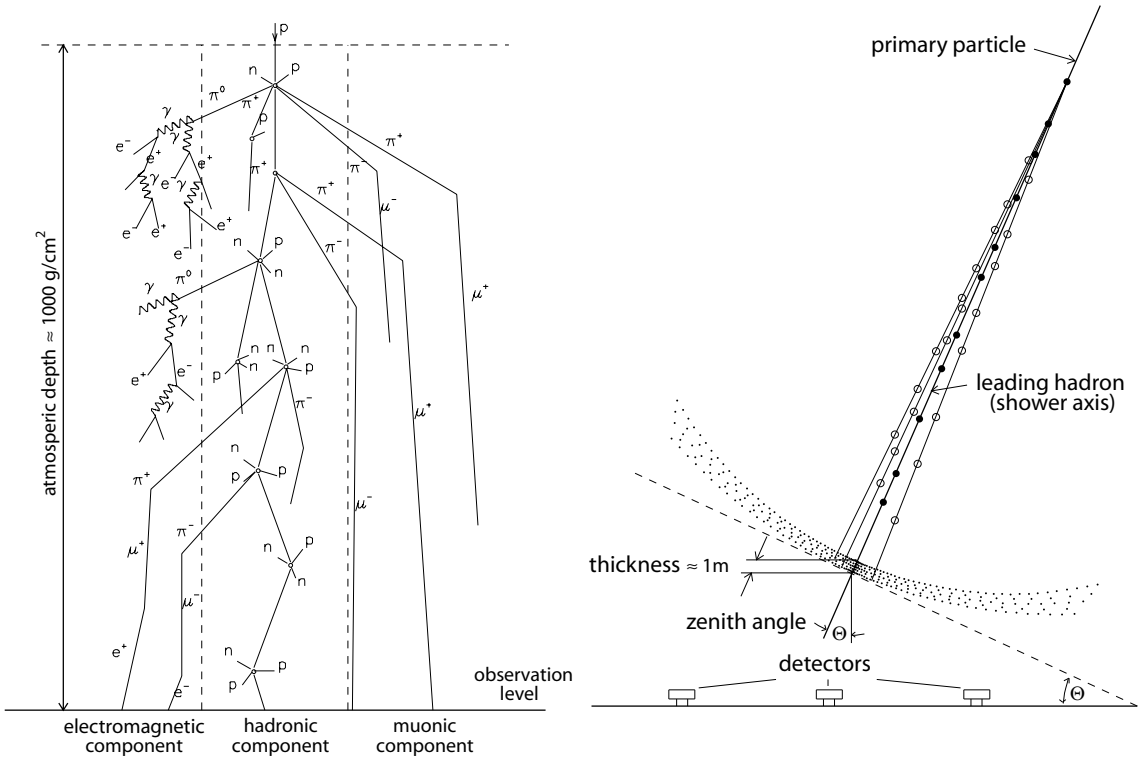

Figure 2.2: Schematic view of an extensive air shower. Left: Development of the different components. Right: Spatial development in the atmosphere.

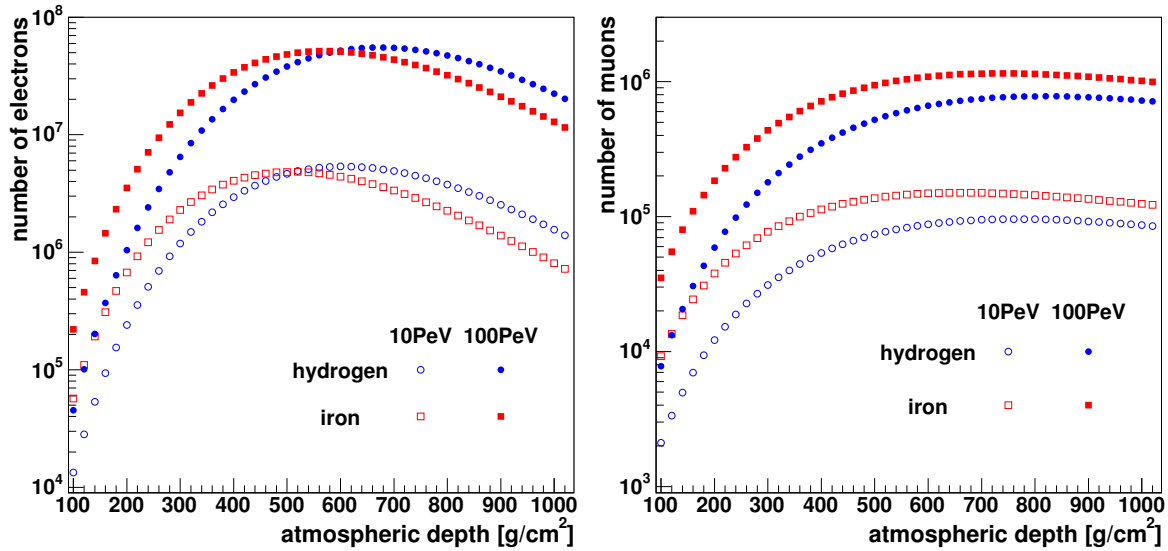

Figure 2.3: Average longitudinal distribution for electrons (left) and muons (right) of 50 simulated air showers for different energies and primaries.

Muonic Component
High energetic muons reaching the ground are often produced in an early stage of the shower development, as at large heights the atmosphere is thin enough that charged mesons can decay before interacting. Low energy muons at ground descend from a later stage in the shower development, typically from a distance of 1km. Muons are rarely submit to Bremsstrahlung as it is strongly suppressed compared to electrons ($(m_\mu/m_e)^2 \approx 40000$), but they loose energy on their way through the atmosphere by ionization. A muon produced at a height of 15 km looses about 2 GeV before reaching ground. Low energetic muons can decay into electrons and neutrinos.

Electromagnetic Component
The electromagnetic component is the most numerous part of an air shower and it origins mainly from the decay of neutral mesons into photons. These photons create by means of pair production electrons, that generate photons by bremsstrahlung. An electromagnetic cascade is initiated. The total number of electrons at a given depth in an air shower initiated by a photon of energy E_0 is given [31] by

$$N_e(t) \sim \frac{0.31}{\sqrt{\beta_0}} \cdot \exp\left(t(1 - \frac{3}{2}\ln s)\right) \tag{2.2}$$

with $\beta_0 = \ln \frac{E_0}{E_c}$, the atmospheric depth $t = \frac{X}{X_0}$ in units of radiation length and the shower age $s = \frac{3t}{t+2\beta_0}$. In air the critical energy for electrons is $E_c \approx 80$ MeV, below this energy the ionization energy-loss mechanisms that does not produce additional shower particles become more important than bremsstrahlung. Thus energy is lost from the shower and the number of particles in the shower decreases as the shower continues to propagate. The parameter s ranges from 0 – 2, the number of particles increases for $s < 1$, reaches a maximum at $s = 1$ and then declines for $s > 1$.
The lateral spread of electrons is largely influenced by Coulomb scattering that is described by the Moliere unit. The lateral distribution of electrons in an electromagnetic shower is described by the so-called NKG formula ([31], [38]),

$$\rho(r) = \frac{N_e}{2\pi \cdot r_m^2} \cdot \left(\frac{r}{r_m}\right)^{s-2} \left(1 + \frac{r}{r_m}\right)^{s-4.5} \cdot \frac{\Gamma(4.5-s)}{\Gamma(s)\Gamma(4.5-2s)}. \tag{2.3}$$

With N_e the number of electrons at observation level, r the distance to the shower core, s the lateral age parameter and $r_m = 78$ m the Moliere unit at sea level.
For air showers initiated by hadrons, the electromagnetic component is a superposition of many electromagnetic cascades with different starting energies and heights. The resulting longitudinal and lateral distribution can be described anyway by functions 2.2 and 2.3 respectively. In that case the age parameter s and the Moliere unit r_m loose their original meaning.

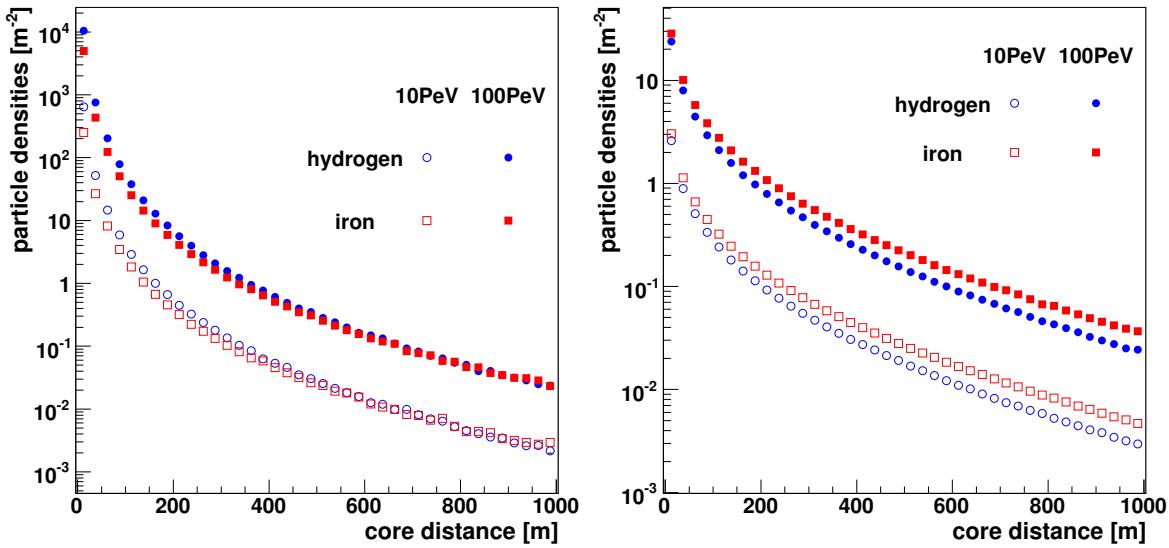

Figure 2.4: Average lateral distribution for electrons (left) and muons (right) of 50 simulated air showers for different energies and primaries.

Different primaries

Air showers of different primary particles develop in different ways and have at ground level different properties, e.g. different electron and muon numbers. Figure 2.3 shows the different longitudinal development of electrons (left) and muons (right) for different energies for hydrogen and iron induced air showers.

At a given energy, the maximum number of electrons is nearly equal, but lies at different atmospheric depths. Iron primaries interact earlier in the atmosphere, therefore the maximum is reached earlier. Higher energetic primaries interact earlier in the atmosphere but have their maximum deeper in the atmosphere. The number of muons increases with increasing atmospheric depth. After reaching the maximum, the muon number decreases very slowly (see Figure 2.3 right).

Figure 2.4 shows the different lateral distributions of electrons (left) and muons (right) for different energies for hydrogen and iron induced air showers. For a given energy the electron lateral distribution of an iron initiated air shower is flatter than for a hydrogen initiated air shower. This is again due to the different shower development of iron and hydrogen initiated air showers. Since iron primaries reach their maximum earlier than hydrogen, their lateral spread increased more when they reach observation level.

The muon lateral distribution shows a similar effect. Iron initiated air showers have their first interaction higher in the atmosphere than hydrogen initiated air showers. Since muons traverse the atmosphere nearly without being deflected, the higher the first interaction occurs the larger is the lateral spread on ground.

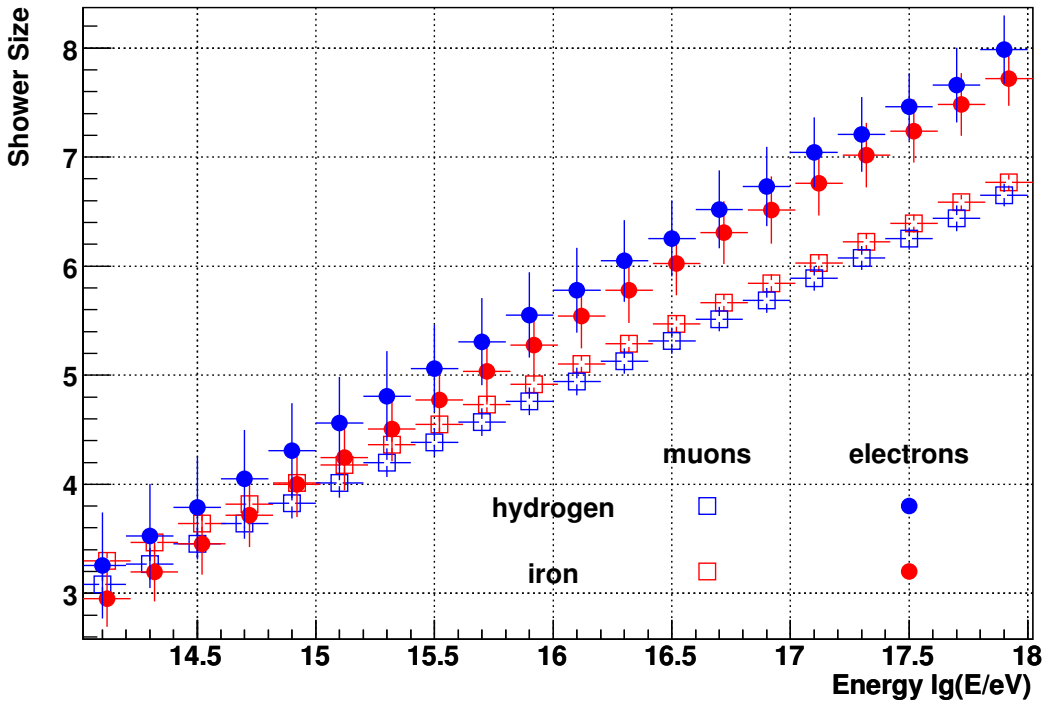

Figure 2.5: Electron and muon shower sizes of hydrogen and iron air shower as a function of primary energy. The error bars show the width of the distribution.

Air showers initiated by higher energetic primaries reach their maximum deeper in the atmosphere and therefore have steeper lateral distributions than lower energetic ones. The muon size is a relatively good energy estimator as can be seen from Picture 2.5. At a given energy the muon size of hydrogen and iron initiated air showers differ by approximately 30%, i.e. $N_\mu^H = 1.3 \cdot N_\mu^{Fe}$ or $\Delta \log N_\mu = 0.15$.
The width of the muon size distribution depends on the primary and decreases with increasing energy. It is always smaller than the difference between hydrogen and iron initiated air showers.
The width of the electron size distribution is at an energy of 10^{16} eV around $\Delta \log N_e = 0.4$, which corresponds to a factor of 2.5. The width decreases with higher energies, at an energy of 10^{17} eV $\Delta \log N_e = 0.3$ which is equivalent to a factor of 2.
In the case of muons, the width of the size distribution at a fix energy is smaller than for a corresponding electron size distribution, which makes it more suitable to estimate the primary energy.

Chapter 3

The KASCADE-Grande Experiment

The KASCADE-Grande Experiment measures Extensive Air Showers induced by cosmic ray particles. The installation is located at Forschungszentrum Karlsruhe, Germany (110 m above sea level, 49.1° N Lat, 8.4° E Long).
One of the major goals of KASCADE is the detailed observation of the primary cosmic ray energy spectrum at energies between 10^{14} eV – 10^{17} eV where a change of the spectral index occurs, the so called knee. Of special interest are the energy spectra of individual mass groups in this energy range. With the extension to the Grande array, extending the accessible energy range to 10^{18} eV, its goal is the unambiguous observation of a knee in the "heavy component", expected in the cosmic ray spectrum at $E_k \approx 10^{17}$ eV.
In order to achieve this goal, the experiment measures of each single event the electromagnetic, muonic and hadronic component of the air shower. Measuring as many observables as possible enables the disentanglement of ambiguities in the reconstruction and analysis of the primary particle.
Figure 3.1 left shows a sketch of the KASCADE-Grande layout, with the Grande array, Piccolo array and the KASCADE experiment. The right part of Figure 3.1 shows the KASCADE experiment with its three main components, the KASCADE array measuring lateral densities and arrival times of the electromagnetic and muonic component, the muon tracking detector that measures tracks of single muons and the central detector measuring high energetic muons and hadrons.
In this chapter a short overview of the different experimental components is given with a focus on the components used in this work. Further information can be found in [10].

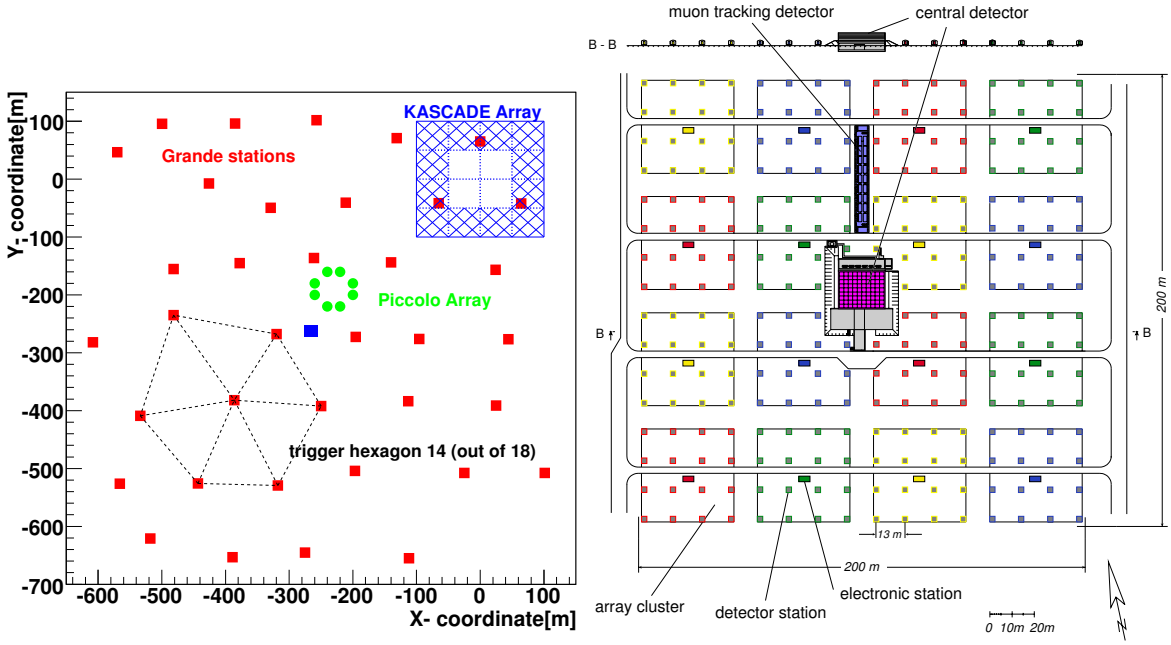

Figure 3.1: Left: Layout of the KASCADE-Grande experiment. Right: Layout of the KASCADE experiment

3.1 The KASCADE Detector Array

The scintillation detectors cover an area of $200 \times 200\text{m}^2$ and are housed in 252 stations on a grid with 13m spacing. They are electronically organized in 16 so-called clusters, the four inner clusters each contain 15 stations because of the central detector. These inner stations are equipped with four e/γ detectors. They have no muon detectors because of the hadronic and electromagnetic punch through close to the shower core. The 12 outer clusters comprise 16 stations that each are equipped with two e/γ detectors and 4 muon detectors.
With a detector coverage of 1.3% and 1.5% for the electromagnetic repsectively muonic detectors, the sampling measurement of the deposited energies enables the measurement of local densities. This enables the reconstruction of the incident angles, lateral distributions and total number of shower particles N_e and N_μ.

Electromagnetic detector
In Fig. 3.2 left, a profile view of a KASCADE Array detector station is presented. Two resp. four e/γ detectors are positioned on a lead/iron plate in a wooden hut. Each e/γ detector consists of a liquid scintillator in a circular tub with 1m diameter and 5 cm height, covered by a light collecting cone. On top a light collector and photomultiplier are mounted to read out the signals. The energy resolution reached is about 8% at 12 MeV, the mean energy deposit of a minimum ionizing particle (m.i.p.).

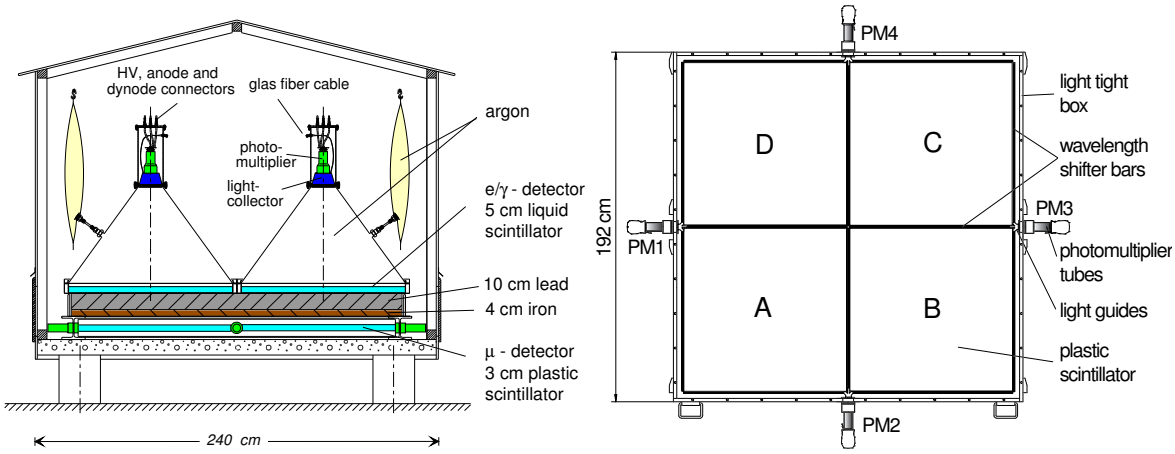

Figure 3.2: Left: Schematic view of a detector station of KASCADE array. Right: Muon detector of detector array

Energy deposits up to an equivalent of 2000 m.i.p. can be detected with a threshold of 0.25m.i.p.. The time resolution has been determined to ≈ 0.8 ns.

Muon Detector
In the 192 outer stations the muon detectors are installed underneath the e/γ detectors and a shielding of 10 cm lead and 4 cm iron, corresponding to 20 radiation lengths. In Fig. 3.2 right the layout of the muon detector underneath the shielding is shown. It contains four plastic scintillators of 3 cm thickness, measuring 90 cm $\times$ 90 cm. The light is coupled out by wavelength shifters and read out by 1.5 inch photomultipliers. The energy resolution has been determined to about 10% at 8 MeV, the mean energy deposit of a m.i.p..

3.2 Central Detector

The central detector consists of several components to measure particle densities in the core of air showers. The main part is a highly segmented hadronic calorimeter [23] with 8 tiers of iron absorber interspersed with 9 layers of warm liquid ionization chambers. Below the third absorber plane a layer of plastic scintillators serves as timing facility and to trigger the read out of other components of the central detector [50]. In the basement underneath the iron and concrete absorbers, two layers of multi-wire proportional chambers [17] and a layer of limited streamer tubes [8] are installed. They measure muons with energies higher than 2.4 GeV by tracking.
On top of the installation, above the first lead filter, the top-layer, a layer of liquid ionization chambers, and the top-cluster, a cluster of scintillation counters, are installed. These two components investigate the e/γ component of low energetic air showers.

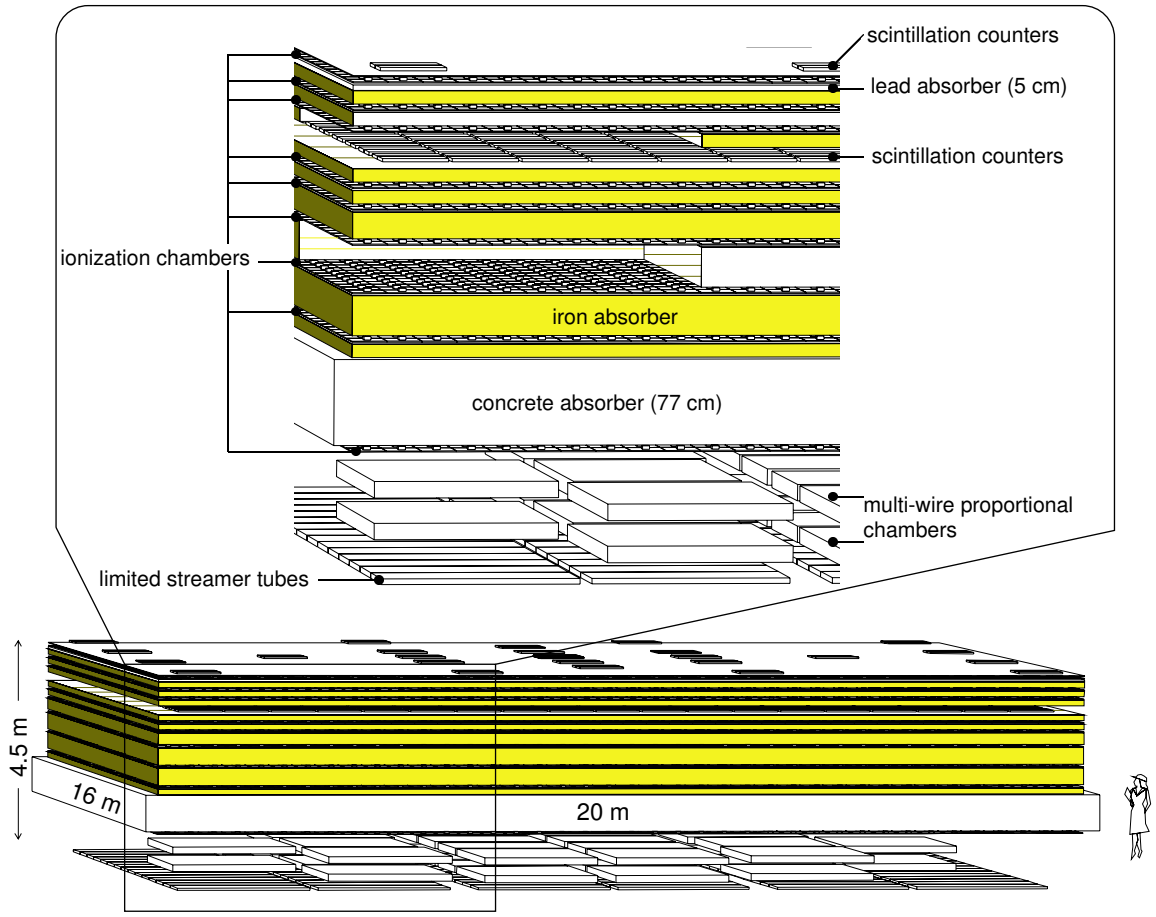

Figure 3.3: Schematic view of the central detector with its components

In Figure 3.3 a schematic view of the central detector is given.

3.3 Muon Tracking Detector

The muon tracking detector[21] is located north of the central detector in a $44 \times 5.4 \times 2.4$ m^3 tunnel, underneath a shielding of concrete, iron and soil corresponding to 18 radiation lengths and a threshold of 0.8 GeV for vertical muons. It houses two rows with 8 detector towers each, each tower consisting of three horizontal and one vertical layer of positional sensitive limited streamer tubes. A schematic view is given in Figure 3.4. With a spacing of 82 cm between the horizontal layers an angular resolution for vertical tracks of 0.3° is obtained. Together with the shower axis it is possible via triangulation to reconstruct the muon production height, which is sensitive to the primary mass of the cosmic ray particle.

3.4 The Grande Array

The Grande array comprises 37 stations with 10 m^2 of scintillation counters — taken from the electromagnetic detector of EAS-TOP[4, 3] — on a collecting area of 0.5 km^2. The stations have an average mutual distance of 137 m.
Each detector is segmented into 16 plastic scintillators measuring 80×80 cm^2 and a thickness of 4 cm. All 16 scintillators are viewed by photomultipliers ($\approx$ 1.6 pC/m.i.p., high gain) whose signals are summed and used for timing and low particle density measurements. The four central scintillators each are seen by an additional photomultiplier ($\approx$ 0.08 pC/m.i.p.) working at a lower gain used for the measurement of highest particle densities. The signals of high gain and low gain are fed into shaping amplifiers, giving two outputs for high gain and one for low gain. This results in measurable particle densities of 0.03–200 m^{-2} for high gain and 20–3000 m^{-2} for low gain.
All 37 stations are connected via 700 m long glass fibers with the Grande-DAQ. Here the stations are electronically connected to 18 hexagonal trigger cells, each consisting of one central plus its six surrounding stations (see Fig. 3.1 left). Hexagon 15 in the S-E corner is an exception, having only 5 outer stations.

3.5 The Piccolo Array

The task of the Piccolo array is to provide a fast trigger to KASCADE and to the Grande array. The Grande array measures events with the shower core outside of KASCADE with too low particle densities within KASCADE to trigger KASCADE components.
Piccolo consists of eight huts, each having 10 m^2 of plastic scintillators. The huts are

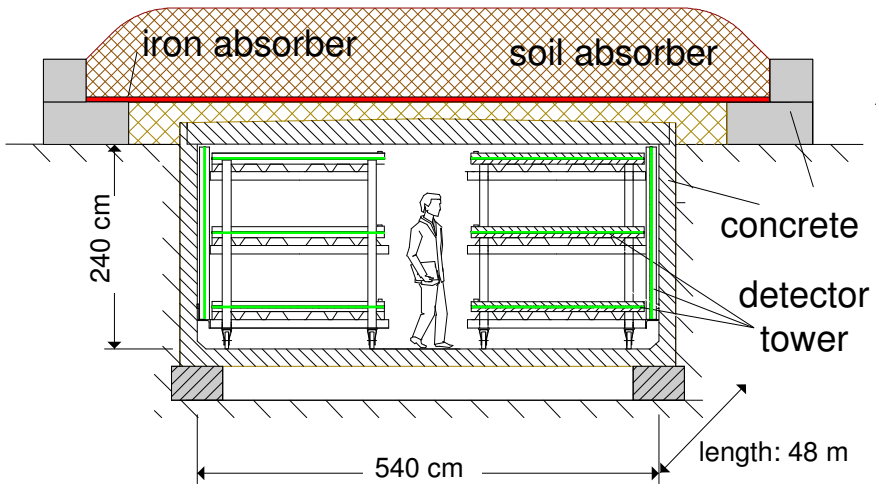

Figure 3.4: Profile view of the muon tracking detector.

Detector	Particle	Area[m^2]	Threshold
Grande array (plastic scintillators)	$e/\gamma + \mu$	370	5 MeV
Piccolo array (plastic scintillators)	$e/\gamma + \mu$	80	5 MeV
KASCADE array (liquid scintil.)	e/γ	490	5 MeV
KASCADE array (plastic scintil.)	μ	622	230 MeV
muon tracking detector (streamer tubes)	μ	4×128	800 MeV
central detector:			
calorimeter (liquid ionization chambers)	h	8×304	50 GeV
trigger layer (plastic scintillators)	μ	208	490 MeV
top cluster (plastic scintillators)	e/γ	23	5 MeV
top layer (liquid ionization chambers)	e/γ	304	5 MeV
multi wire proportional chambers	μ	2×129	2.4 GeV
limited streamer tubes	μ	250	2.4 GeV

Table 3.1: Detector components of KASCADE-Grande, their total sensitive area and threshold for vertical particles

placed on an octagon, with a distance of 20 m to each other. Each hut is divided in two stations, each station comprises six scintillators. The trigger conditions can be chosen as double multiplicity trigger (n out of 8 huts and m out of 48 electronic channels). One electronic channel is made up of the summed signal of the photomultipliers viewing two scintillators, thus three channels per station, six per hut. The trigger condition used is $n = 2$ and $m = 4$.
Table 3.1 summarizes the most important characteristics of the different detector components of KASCADE-Grande.
Figure 3.5 shows the distribution of energy deposits and arrival times in the Grande detector for an air shower with a primary energy of approximately 3×10^{16} eV. One recognizes the position of the shower core close to the stations with highest energy deposits. From the arrival time distribution one sees the different times of flight through the atmosphere for the particles. The shower axis can be seen as approximately perpendicular to the arrival time distribution.

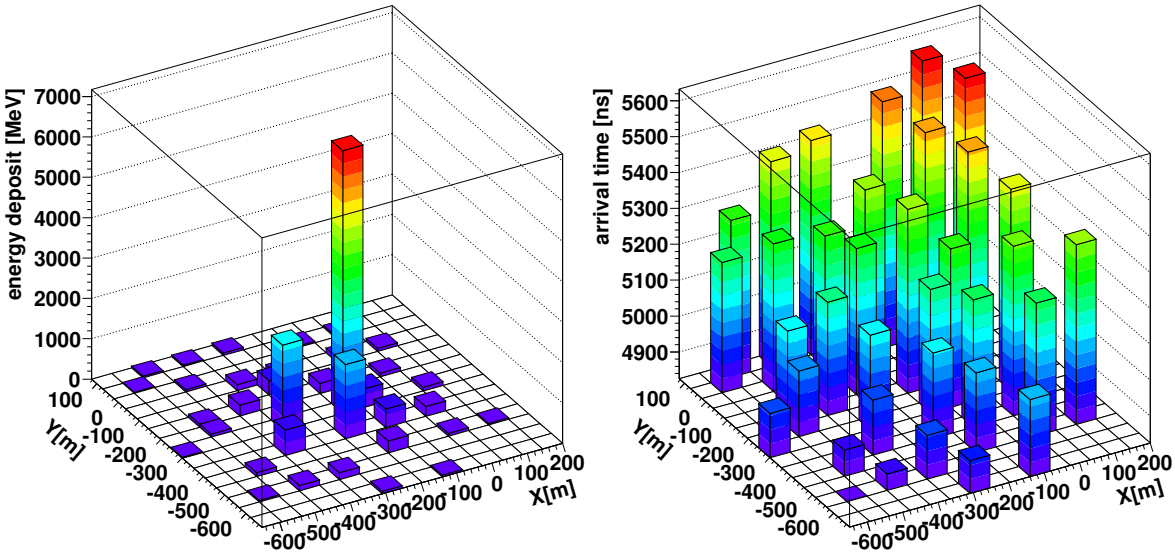

Figure 3.5: Energy deposits (left) and arrival times (right) in the Grande detector for a measured extensive air shower. The reconstructed parameters for this event are: zenith angle $\theta = 16°$, azimuth angle $\Phi = 244°$, $\log_{10} N_e = 6.7$ and $\log_{10} N_\mu = 5.4$.

Chapter 4

Reconstruction of Air Showers

4.1 Simulation of Extensive Air Showers

To understand and interpret correctly the measurements of extensive air showers their simulation is necessary. The program CORSIKA [34] (COsmic Ray SImulations for KAscade), developed in Karlsruhe, uses Monte-Carlo methods to describe the development of an extensive air shower initiated by high energy cosmic ray particles. Primary and secondary particles are tracked until they reach ground, their energy falls below an adjustable energy threshold, until they undergo reactions with air nuclei, or until they decay. In particle decays all decay branches down to the 1 % level are taken into account.
The description of hadronic interactions is divided in two parts, low and high energetic hadron interactions with an adjustable transition energy. For both the low and high energy range different interaction models can be chosen, which allows to estimate their systematics effects on air shower observables.
For simulations used in this work CORSIKA 6.156 with FLUKA 2002.4 [26] was used to describe low energetic hadronic interactions up to energies of 200 GeV. Higher energy interactions are handled by QGSJET [37]. The electromagnetic component is described by EGS4 [45], which is implemented in CORSIKA.
The used simulations comprise 9 sets of energy spectra from 10^{14} eV to 10^{18} eV with a spectral index of $\gamma = -2$. One set consists of approximately 64000 simulated air showers for five primaries: hydrogen, helium, carbon, silicon, and iron. The zenith angle covers a range from 0° to 42°. The first two sets were used five times with different shower cores as input for further simulation of the detector response, the seven following sets were used ten times.
The simulated air shower events are spread uniformly over an area of 760×800 m^2 and used as input for the GEANT3 [18] based detector simulation CRES (Cosmic Ray Event Simulation). CRES is the program for the simulation of the signals and energy deposits in all detector components of KASCADE as response to an extensive

air shower. It accounts for the physical behavior of active and passive detector parts and the exact geometry of the detectors. Its output is in the same format as the raw data from the experiment and can be analyzed in an identical way by the software KRETA.

4.2 Overview of the Reconstruction Algorithm

The reconstruction of air shower events at the KASCADE-Grande experiment is done in three levels, as it is illustrated by the flow chart in Fig 4.1.
The observables used are the measured ADC and TDC channels measured by the Grande array. These are converted to deposited energies and time values as seen in the previous chapter in Figure 3.5. From these the reconstruction software KRETA (KASCADE REconstruction for exTensive Air showers) reconstructs the physical quantities, e.g. core coordinates, arrival direction (Φ, Θ), and number of electrons, of muons, of hadrons, etc..
Here the focus will be put on the the description of reconstruction algorithms used for an event where the Grande array has data, i.e. is part of an event. For an event where the Grande array is not part of the event the standard KASCADE reconstruction is followed, also done in three levels with slightly different algorithms as described in [9].

Level 1
In the first level rough estimates of shower core, arrival direction and shower sizes are determined in a robust way. These serve as starting values for the second level reconstruction algorithms, therefore the first level provides always results.
The shower core is determined by a center of gravity method, where the coordinates of a station are weighted with the measured energy deposit. Naturally the core obtained with this method can only be within the grid defined by the stations.
The arrival direction can be reconstructed in two ways: First the shower direction can be obtained by calculating the shower front as a plane in an iterative procedure using the arrival times of the three stations with the highest energy deposit. In the second method, the standard way, the arrival times of all stations are used and weighted with the locally measured particle densities. The arrival times of the 1st particle are compared with an average particle arrival time at a given shower radius for the measured number of particles, derived from simulations. The average arrival time is assigned with a width proportional to square root of the total number of particles. For this method the shower core has to be known, the first one is also applicable without a known core position.
A first estimate of the number of charged particles is obtained by summing up the number of measured particles and of the expected particles at the given radius. The lateral distribution function used has a fixed age. The estimate is the ratio of the measured to the expected sum of particles. The muon number is estimated by using the

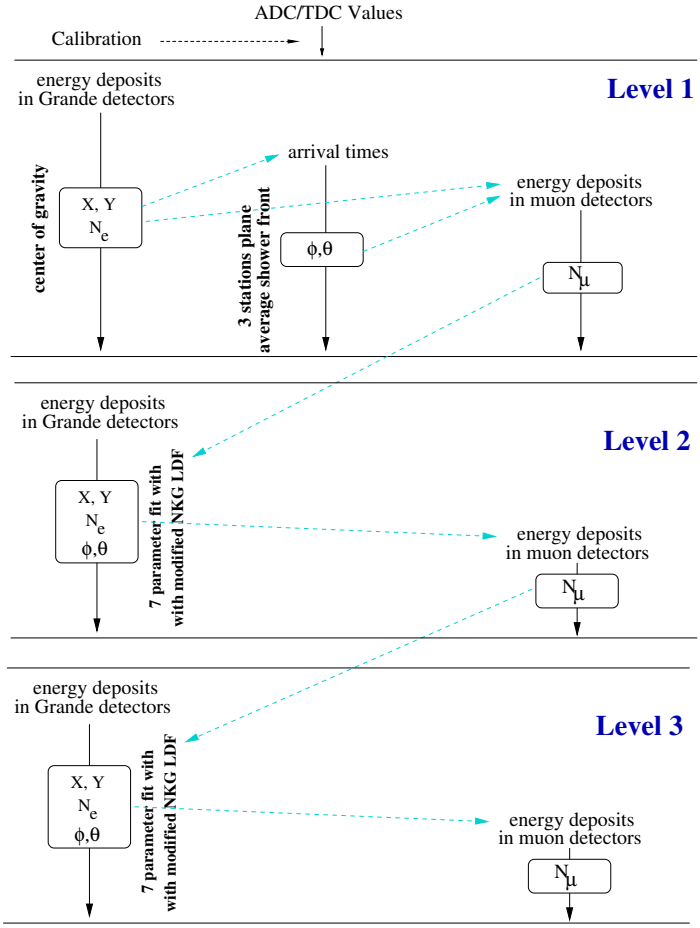

Figure 4.1: Schematic view of Reconstruction at KASCADE-Grande.

energy deposits measured in the muon detectors of the KASCADE array and fitting them with a lateral distribution function with a fixed shape.

Level 2

From this level on, the reconstruction of the shower parameters is done in the shower coordinate system, where the shower axis is perpendicular to the X-Y plane. To describe the lateral distribution of electrons in air showers measured with KASCADE-Grande, up to radial distances of 800 m, a slightly modified NKG-function is used [12].

$$\rho(r) = \frac{N_e}{2\pi \cdot r_m^2} \cdot \left(\frac{r}{r_m}\right)^{s-\alpha} \left(1 + \frac{r}{r_m}\right)^{s-\beta} \cdot \frac{\Gamma(\beta - s)}{\Gamma(s - \alpha + 2)\Gamma(\alpha + \beta - 2 - 2s)}. \quad (4.1)$$

The parameters $\alpha = 1.5$, $\beta = 3.6$ and $r_m = 40$ m were found to be the optimum describing the measured electron densities within the radial distances relevant

for KASCADE Grande. Compared to the common parameters of KASCADE with $\alpha = 2, \beta = 4.5$ and $r_m = 89$ m, the age parameter is shifted to the theoretical range of -0.4 to 1.5. As both, the function to describe the lateral distribution and the function to describe the average arrival time are coupled through the used core coordinates and local particle numbers, they are fitted simultaneously in a negative-log-likelihood minimization. The contribution of the muons is taken into account with the muon number reconstructed at level 1 and the lateral distribution used there.
In the minimization procedure seven free parameters are fitted, core coordinates, arrival direction and electron number and shower age [29]. With the improved shower direction and core position the muon number is reconstructed again in the same procedure.

Level 3
In this level the electron lateral distribution is reconstructed taking into account the improved muon component from the previous level. This results in a more precise shower core, direction and electron number. Hence the muon lateral distribution is fitted again using the improved core position, which results in a slightly improved muon number compared to the previous level. At this level the parameters of an air shower are reconstructed with highest precision and can be used for analyses.
In the following the reconstruction qualities and systematic effects will be discussed by studying Monte Carlo simulations.

4.3 The Lateral Energy Correction Function

In order to reconstruct the shower sizes one has to know the particle densities measured in the detectors. These are obtained by converting the measured energy deposits to particle numbers by means of conversion functions. The energy deposits in the scintillator detectors are dominated by ionization losses of shower electrons and muons. However, there is an additional contribution to the measured total energy deposit from the conversion of the shower gamma component and from hadrons especially close to the shower core.
A Lateral Energy Correction Function (LECF) is derived from simulated air showers based on CORSIKA [34] and a detailed GEANT [18] detector simulation. For the Grande detector this function gives the average energy deposit per charged lepton at a given core distance (see Fig. 4.2 left). For increasing radii one sees an increase of energy deposit per charged lepton which is due to an increase of the gamma to electron ratio. Air showers that are initiated by heavier elements, e.g. iron, deposit in average few percents more energy per lepton because they have their first interaction higher in the atmosphere and the lower energetic part of particles are lost. Likewise air showers initiated by higher energetic primaries, that penetrate deeper into the atmosphere deposit in average few percent less energy per particle.

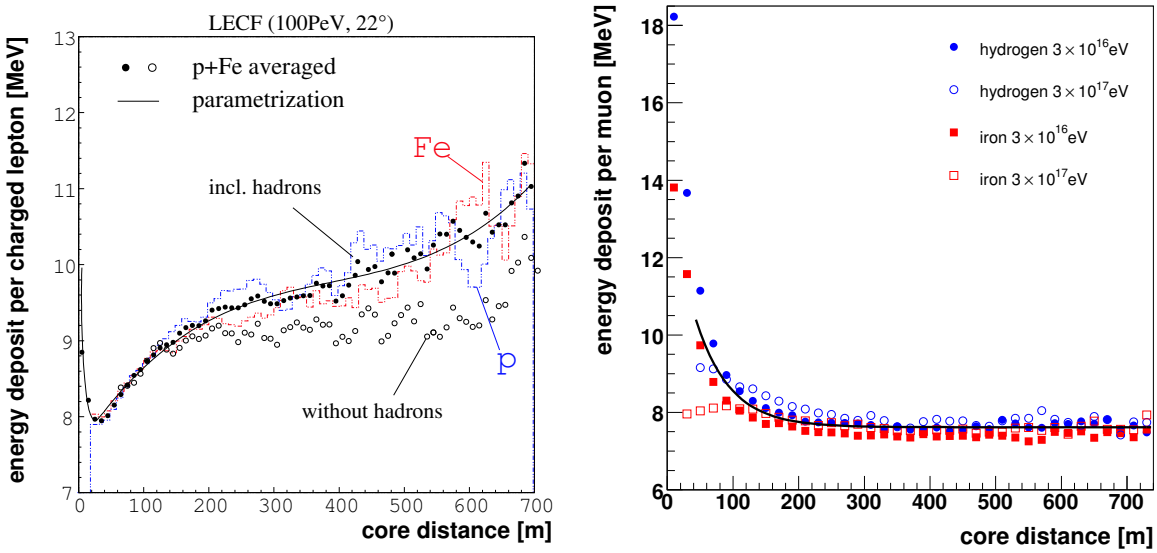

Figure 4.2: Left: Average energy deposit of an extensive air shower (hydrogen and iron, 100 PeV, 22°)[28]. Right: Average energy deposit per muon. (Hydrogen and iron, 22°. The shown function is obtained as average of 30 PeV, 100 PeV, and 300 PeV) air showers.

For the muon detector of the KASCADE Array the LECF has been determined based on two primaries and three different simulated energies, 3×10^{16} eV, 10^{17} eV and 3×10^{17} eV. For reasons of clarity in the right part of Figure 4.2 only the values for 3×10^{16} eV and 3×10^{17} eV are shown. As one can see in Figure 4.2 right the above mentioned difference between the two primary particle types and different primary energies is not significant above a level of 5% and therefore can be averaged by the function 4.2,

$$\frac{E_{dep}}{\text{muon}}(r) = (7.617 + \exp(1.862 - 0.0193 \cdot r))\text{MeV} \tag{4.2}$$

with the radius r in meters. This function gives the average energy deposit per shower muon in a radial range of 40 m to 800 m. For small radii up to approximately 160 m one sees a decrease due to high energetic electromagnetic punch through, which is corrected for by function 4.2. At larger radii the deposited energy per muon reaches a constant value of approximately 7.6 MeV.

4.4 Reconstruction of the Muon Size

Since the detectors of the Grande array have no shielding, they measure the electromagnetic component together with the muon component of an air shower.
In order to discriminate between energy spectra of different mass groups it is impor-

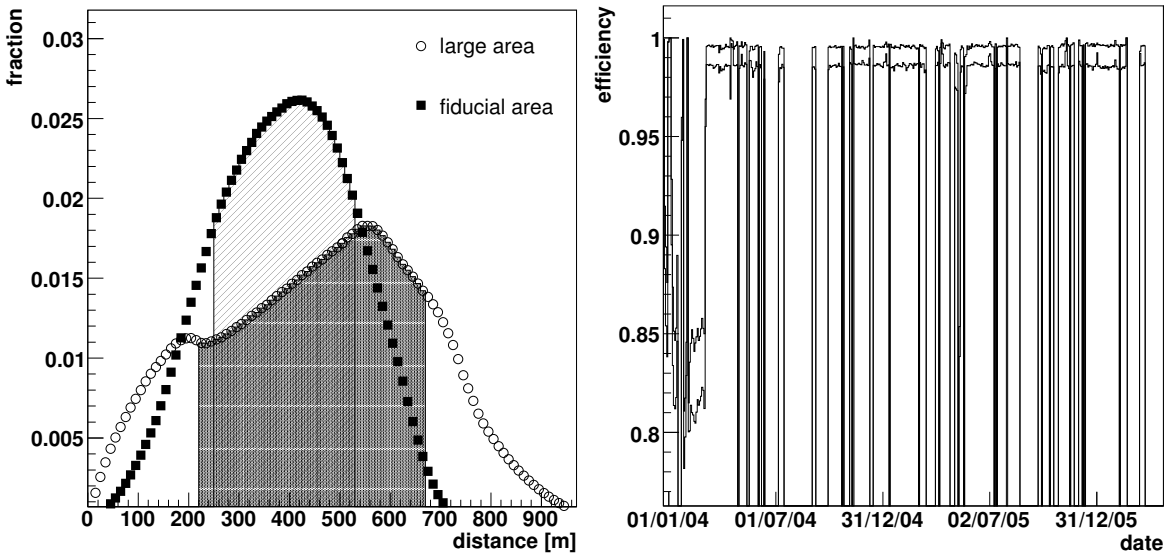

Figure 4.3: Left: Distance Distribution of muon detectors to shower core for different areas. Large area means 760×800 m^2 and fiducial area a circle with 250 m radius around center of Grande array. Right: Efficiency in reconstructing muon number over time without any cuts and including reconstruction cuts.

tant to measure the electron and muon number of an event (see Fig. 2.5). Using the muon detectors of the KASCADE array it is possible to reconstruct the number of muons for an event that triggered the Grande array.
As described in Chapter 3.1 the KASCADE array provides 622 m^2 of plastic scintillator detector that can measure muons above an energy threshold of 230 MeV. The dimensions of the KASCADE array allow the measurement of the muon density over a radial range of up to 280 m. Given the arrangement of the KASCADE array with respect to the Grande array, the distance of the muon detectors of the KASCADE array to the shower cores ranges from 0 m to 800 m. The left part of Figure 4.3 shows the distance distribution of muon detectors to the shower core for events within a given area, with the shaded area being the radial range in which the measurement of the muon density occurs for 68% of the measured showers. The radial range where the muon density is measured depends on the chosen fiducial area. It ranges from 250 m to 530 m for the chosen fiducial area of a circle with radius of 250 m around the center of the Grande array.
In Figure 4.3 right the efficiency in reconstructing the muon size of an air shower is shown. The lower at 98.5% curve shows the efficiency in reconstructing the muon number for any event triggering the Grande array, provided that the KASCADE array is running and none of the outer clusters is missing. The higher curve at around 99.5% shows how the efficiency increases when one includes further necessary reconstruction

cuts, i.e. a minimum of 19 stations with an energy deposit and a valid shower age for the electromagnetic lateral distribution.
Due to hardware problems with a trigger cable in the KASCADE array the first few months of data taking show a lower efficiency of around 80–85% for reconstructing the muon number. The corresponding data are not used in the later discussed muon size spectrum and its unfolding.
The reconstruction methods for the muon size were studied by reading simulated muon distributions on ground plane at the location of the KASCADE array for shower cores spread over the Grande array. The chosen function 4.3 to describe the measured muon lateral distribution is similar to the one proposed in Ref.[43] for the electron component.

$$\rho_\mu(r) = \mathrm{N}_\mu \cdot f(r) \text{ , with } f(r) = \frac{0.28}{r_0^2}\left(\frac{r}{r_0}\right)^{p1} \cdot \left(1+\frac{r}{r_0}\right)^{p2} \cdot \left(1+\left(\frac{r}{10\cdot r_0}\right)^2\right)^{p3} . \quad (4.3)$$

The parameters $p1$, $p2$, $p3$ were obtained to be -0.69, -2.39 and -1.0 respectively averaging the fit results of the lateral distribution function to 10^{16} eV and 10^{17} eV proton and iron induced air showers. A fix scaling radius of $r_0 = 320$ m is used. Because of the low measured muon densities and in order to obtain stable fit results, the curvature of the lateral muon densities is kept constant and only the muon number N_μ is estimated by $N_\mu^{est} = \sum_i n_i / \sum_i (f(r_i) \cdot \mathrm{A}_i \cdot cos(\theta))$. Where n_i are the number of particles measured in a core distance r_i within an area A_i and θ is the zenith angle of the air shower. Due to punch through of the electromagnetic component close to the shower core, an inner radial cut of $r_i > 40$ m is applied.
The assumption of a fixed shape parameter introduces a small systematic difference for different primaries, since the shape of the lateral distribution depends slightly on the primary. As can be seen in Figure 4.5 right the systematic difference between hydrogen and iron induced air shower is smaller than 5%.

4.5 Reconstruction Qualities

In the following the qualities of reconstruction are compared with two sets of simulation. The first is the standard simulations described in Section 4.1, the second is a new set of simulations that includes a higher contribution from electronic effects from Grande detectors. This second set describes the resolution obtained with the Grande detectors more realistically. The part of the second set used for the studies described in this section is an average of hydrogen and iron primaries. Comparisons to the first set are anyway shown because a much higher statistic is available, which is needed for the work shown in Chapter 6 and Chapter 7, where the muon size is used.
As will be shown in Chapter 4.5.2 the quality of reconstruction of the muon size is

affected only weakly by the electronic effects from Grande detectors.
The following cuts are used for the discussion of reconstruction qualities:

- A minimum of 20 stations for the Grande array measured an energy deposit.
- The reconstructed shower core lies within a fiducial defined by a circle with 250 m radius around the center of the Grande array.
- The age parameter of the lateral distribution that describes the measured electron density distribution lies in the range of 0.4–1.4.
- The zenith angle is in the range 0° – 25°.

4.5.1 Core and Angular Resolution

For the reconstruction of the muon component of an air shower event, the precision of the core position and arrival direction are important. The reconstruction qualities are studied with Monte Carlo simulations, where the reconstructed parameters can be compared to the originally simulated ones.
The used events need to have triggered the Grande array and fulfilled the specified reconstruction cuts to be considered a successfully measured and reconstructed event. In Figure 4.4 (left) the core resolution is shown in dependence of the shower size for two different primary particles. One sees that the precision increases with shower size, i.e. $\Delta r \propto N_e^{-\alpha}$ and that the precision is nearly independent for the primary. For showers that have more than 10^6 electrons, which corresponds to 100 % efficiency, the spatial resolution ranges from $\approx$ 10 m to $\approx$ 2 m for air showers with around 10^8 electrons.
The angular resolution as function of shower size is shown in Figure 4.4 right, no dependence on the primary is seen. At trigger threshold it amounts to around 0.3° and decreases with increasing electron number.
The new set of simulations, which includes a higher contribution from electronic noise, shows a core resolution of around 12 m and an angular resolution of 0.6°. As can be seen in the following chapter this has no large effects on the precision of the reconstructed muon size.

4.5.2 Reconstruction Quality of Shower Sizes

The reconstructed shower sizes for a single event are not necessarily identical to the true values of an air shower. Possible reasons are statistical fluctuations within the shower disc that differ from their theoretical expectations and systematic effects that can be e.g. due to a not 100% correct conversion of energy deposit to particle densities or in the description of the lateral density distribution.

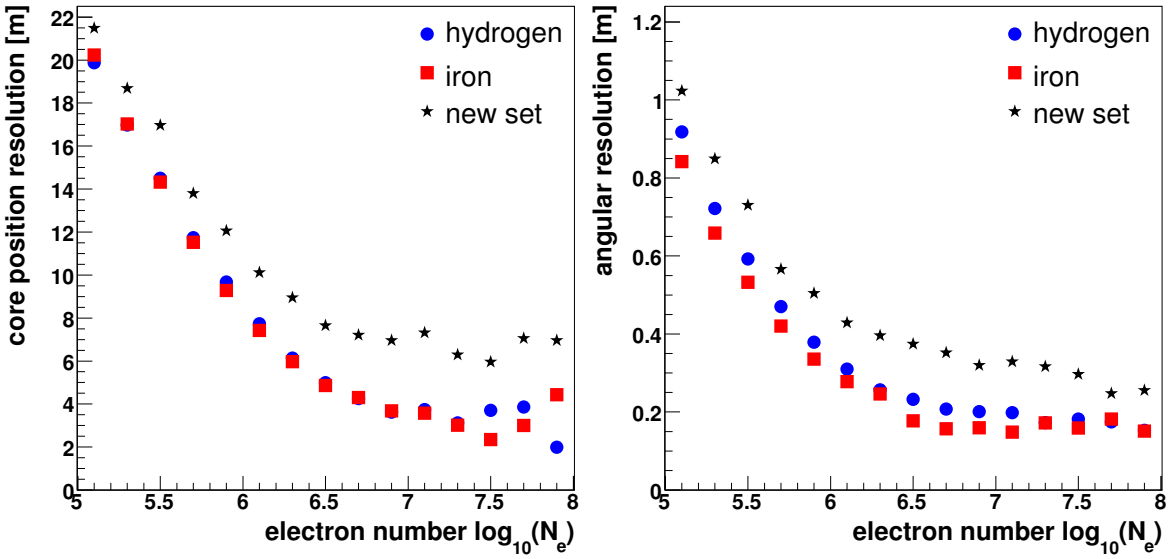

Figure 4.4: Accuracy of reconstruction of the shower core (left) and of the arrival direction (right) in dependence of shower size.

To study the precision of the reconstruction of shower sizes one use simulations for which a comparison of reconstructed and true values is possible. The accuracies for the reconstructed shower sizes are displayed in Figure 4.5, where the differences of the reconstructed and true logarithmic shower sizes are shown. The mean values correspond to the systematic deviation and the width of the distribution to the statistical uncertainty. One sees for the electron number that above threshold at 10^6 electrons the systematic deviation follows a trend of 0% to -10% at highest energies. The statistical uncertainty decreases from around 30% to 15% with increasing shower size. For shower sizes larger than 10^7 electrons one observes a flattening in the statistical uncertainty due to saturation effects of detectors close the shower core. For the set of simulations including electronic effects the statistical uncertainty remains larger at around 20%. The muon number shows above threshold a decrease of the systematic error from 10% to 0% with increasing muon number. The statical uncertainty decreases from around 30% to 10% for large shower sizes. Showers below 100% efficiency are characterized by a rather large statistical uncertainty of 60% to 80%. Together with the steep cosmic ray spectrum this causes an overestimate of the flux in the muon size spectrum in the range of $\log_{10} N_\mu = 5$ to $\log_{10} N_\mu \approx 5.5$.
For both electron and muon shower sizes the systematic deviations always stay well below the statistical accuracy. The new set of simulations does not influence the reconstruction quality of the muon number. One can see that the statistical and systematic uncertainties agree very well with the standard set of simulations.
In Figure 4.6 the accuracies of the reconstructed muon number is shown as function of

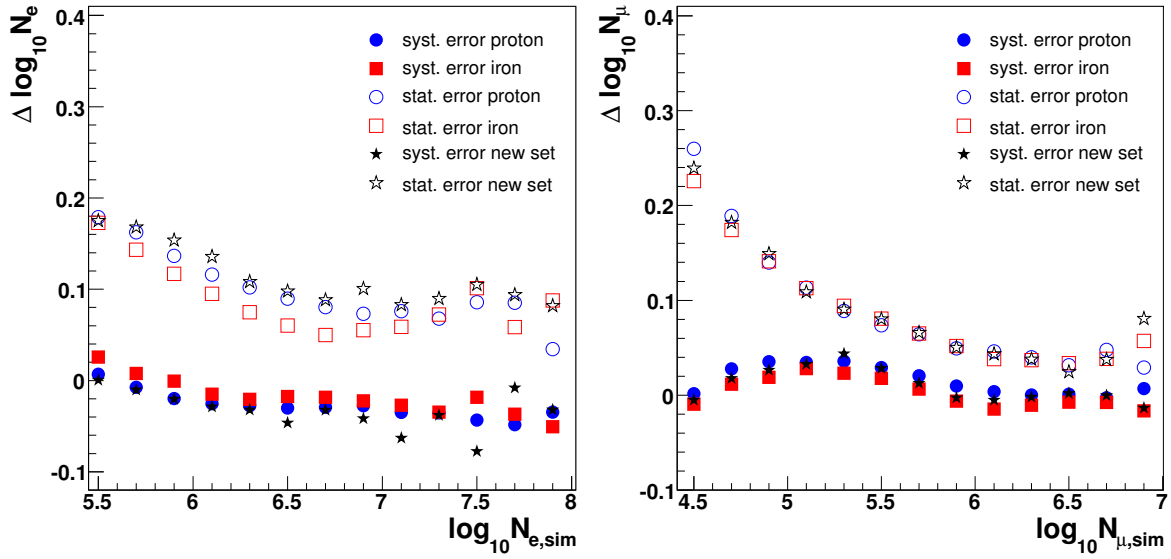

Figure 4.5: Quality of reconstruction of electron number (left) and muon number (right) for simulated air showers. Shown are systematic and statistical uncertainties as function of respective shower size.

distance to the KASCADE array. The left part of Fig. 4.6 represents all showers that pass the standard reconstruction cuts. One sees for increasing distances an increase of the statistical uncertainty to approximately 100%. In the right part of Fig. 4.6 a minimum electron number of $\log_{10} N_\mu > 5.$ is required, which corresponds to 100% efficiency. An increase of the statistical uncertainty with increasing distances, from approximately 10% at 100 m distance to 30% at 600 m distance, is observed. The systematic uncertainties increase for larger distances to the KASCADE array, up to 20% at 600 m.

4.6 The Reconstruction Efficiency

For the understanding of the data not only the reconstruction precision and systematic effects are necessary but it is also important to know at what energies and shower sizes an air shower triggers the array and is measured. The Grande array is electronically divided in 18 overlapping hexagons (see Chapter 3.4). The trigger condition for the Grande array to trigger itself is a coincidence in one hexagon consisting of seven stations. Furthermore it can be triggered by the Piccolo array (see Chapter 3.5).
The Grande stations are sensitive to the charged component of an air shower, with the electromagnetic component being most numerous. Thus one expects that the trigger efficiency depends mainly on the number of electrons which can be seen in the left part of Figure 4.7, where the trigger efficiency is shown in dependency of $\log_{10} N_e$ for

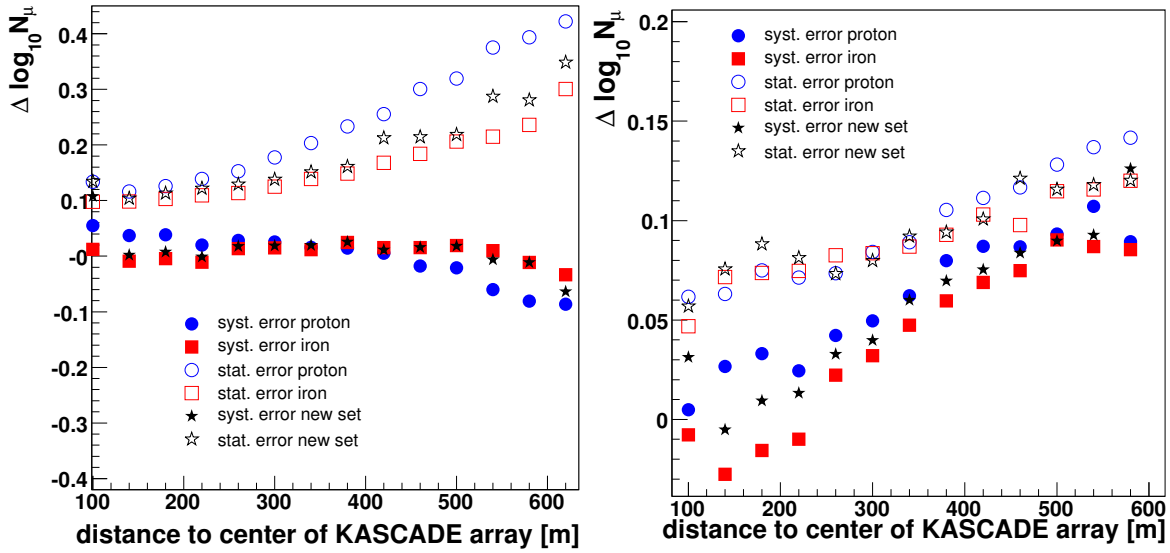

Figure 4.6: Quality of reconstruction of muon number as function of distance to the KASCADE array. Left: Using standard reconstruction cuts. Right: Requiring $\log_{10} N_\mu > 5$, in order to be at 100% efficiency.

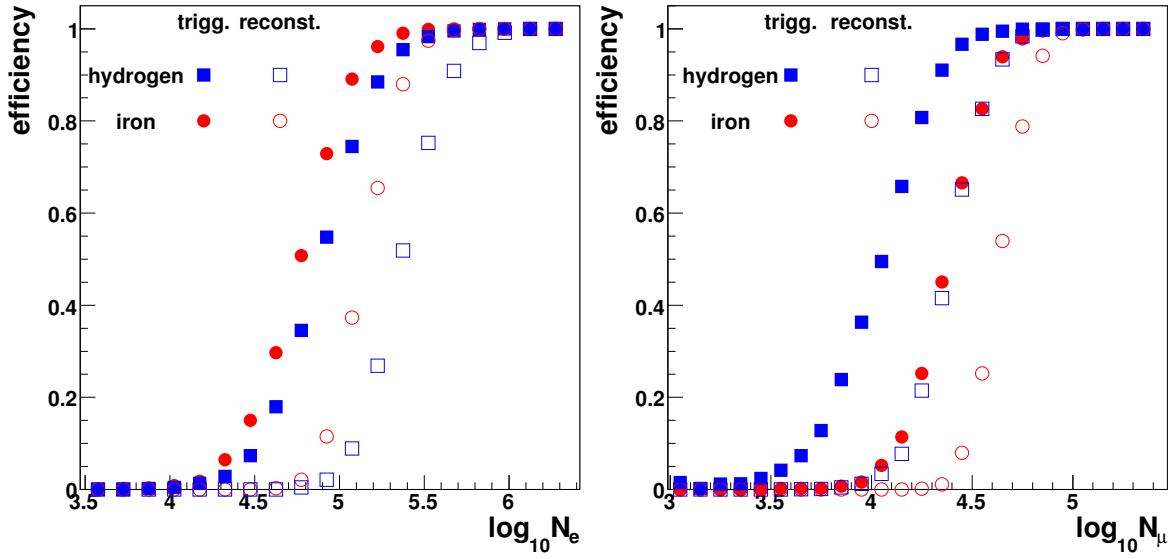

Figure 4.7: Trigger and Reconstruction efficiency for Hydrogen and Iron induced air showers (0°–18°) as function of electron number (left) and muon number (right).

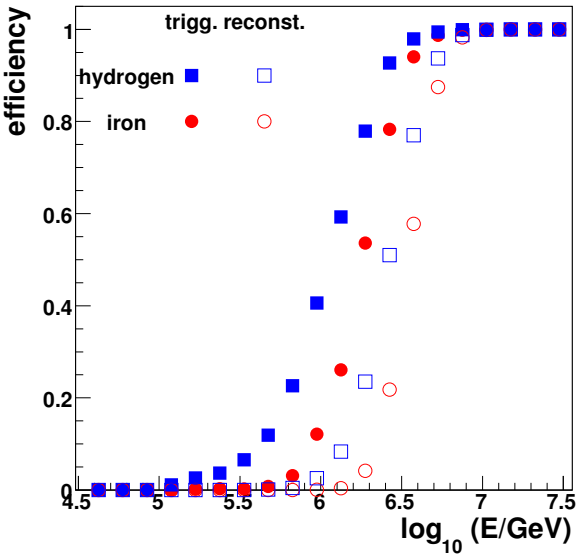

Figure 4.8: Trigger and Reconstruction efficiency for Hydrogen and Iron induced air showers (0°–18°) as function of primary energy.

air showers with zenith angles smaller than 18°. There is no large difference between the two considered primaries hydrogen and iron, both reach 100% efficiency at an electron number of $\log_{10} N_e \approx 5.7$. For iron induced showers the efficiency is slightly higher as for protons. This is due to a higher energetic gamma component at same electron numbers which yields in a higher energy deposit in the Grande detectors. Furthermore, at a given electron an iron initiated air shower has more muons than a hydrogen initiated air shower. These muon also contribute to the energy deposit in Grande detectors. Also shown in the left Figure 4.7 is the reconstruction efficiency within the fiducial area, which implies a minimum number of 19 stations in an event and a successfully reconstructed muon number. The last condition introduces a higher sensitivity to the primary. For Iron induced air showers 100% efficiency is reached at $\log_{10} N_e \approx 5.7$ and for Hydrogen at $\log_{10} N_e \approx 6$.
The efficiency in dependency of the muon size is shown in the right part of Figure 4.7. Hydrogen induced air showers reach 100% efficiency in average at $\Delta \log_{10} N_\mu \approx 0.3$ lower muon numbers than iron due to their more numerous electromagnetic component. At a muon number of $\log_{10} N_\mu \approx 4.7$ 100% efficiency for any kind of primary is reached and for $\log_{10} N_\mu \approx 5.0$ a successful reconstruction is sure. Figure 4.8 shows the reconstruction efficiency for air showers with zenith angles smaller than 18° as function of the primary energy. Hydrogen induced air showers start triggering at slightly lower energies but for all air showers full efficiency is reached at an energy of approximately 10^{16} eV.

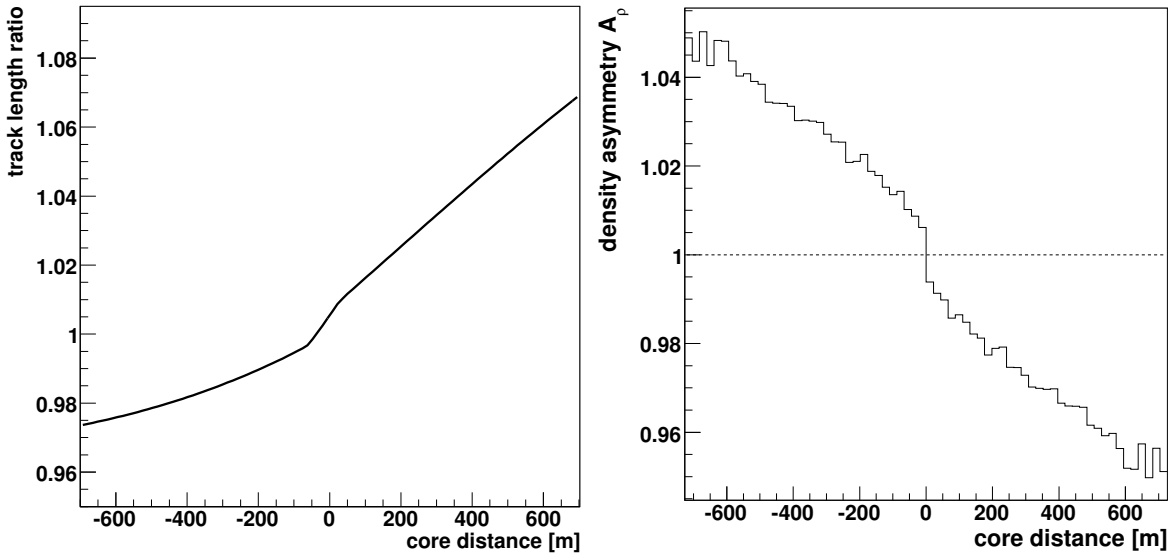

Figure 4.9: Left: Ratio of true and assumed track lengths in detector in dependency of core distance above and below shower axis. Right: Asymmetry A_ρ in muon density in dependency of core distance above and below shower axis. For both are shown average values of 10^{17} eV hydrogen and iron initiated air showers with $\theta = 22°$.

4.7 Asymmetries in Shower

The KASCADE array does not have the same center as the Grande array. In fact, the central point of the KASCADE array is shifted by around 360 m to the North-East from the center of the Grande array. Due to this arrangement, for showers coming from a certain direction the measurement of the muon density occurs in average mostly below or above the shower axis. Above the shower axis means in direction of the shower axis towards ground, looking up. The measurement of the muon density occurs for showers coming from South West mostly above shower axis, for showers coming from North East it occurs mostly below.
There are two competing effects that can cause a change of the measured density. First there is the track length of the muons in the detector and second attenuation effects due to the path lengths in the atmosphere. At larger core distances the average muons do not fly necessarily parallel to the shower axis but are inclined towards it. Figure 4.9 left shows the ratio of the true track length and the used track length in reconstruction in the detector for 10^{17} eV air showers. The average of 40 hydrogen and 40 iron induced air showers with a zenith angle of $\theta = 22°$ is used for this graph. The distribution of zenith angles α of muons in the detector on ground plane in dependency of the the core distance is determined at first. Negative and positive core distances correspond to, respectively, below and above the shower axis. The track

length is given by $1/\cos\alpha$, which is compared to the track length suggested by the measured shower axis with zenith angle θ. Thus the ratio shown in Fig. 4.9 left is given by $\cos(\theta)/\cos(\alpha)$. For large radial distances the underestimate is up to around 2% and the overestimate up to 6%.
On the other hand the attenuation in the atmosphere has an opposite effect, as indicated by the graph on the right in Fig. 4.9, determined with 40 hydrogen and 40 iron induced air showers. Here the density asymmetry A_ρ as function of distance to the shower core below and above shower axis is represented. A_ρ is given by

$$A_\rho(r) = 1 + \frac{\rho(r)_{below} - \rho(r)_{above}}{\rho(r)_{below} + \rho(r)_{above}} \tag{4.4}$$

with r the distance to the shower core. Below the shower axis particles have a shorter path through the atmosphere and are less affected by attenuation, which results in a 5% higher density at a distance of 600 m to the shower axis. Above shower axis instead they have to traverse more matter and the density at 600 m distance is reduced by 5%. With a maximum of 6% the mentioned effects are relatively small for a shower with a zenith angle $\theta = 22°$.
In Figure 4.10 the measured mean muon numbers for various zenith angle ranges are shown as a function of the azimuth angle. In the left part of Figure 4.10 no cut on a minimum efficiency was applied, also showers close to the threshold are included. One observes an effect that gets more significant with increasing zenith angle, which is also due to the trigger threshold being sensitive to the azimuth angle because of the geomagnetic field. As the right part of Fig. 4.10 shows, no significant effect is visible for showers with a minimum electron number of $\log_{10} N_e > 6$, which corresponds to 100% efficiency.

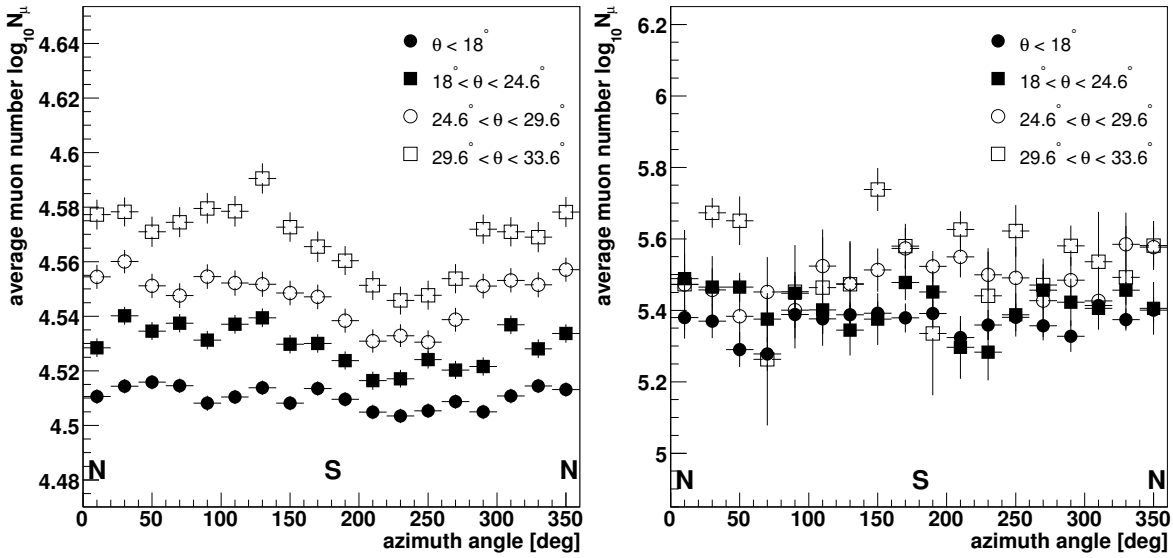

Figure 4.10: Measured muon size as function of azimuth angle. Left: Without a cut on minimum efficiency. Right: Requiring $\log_{10} N_e > 6.$ in order to be at 100% efficiency.

Chapter 5

Measured Data

In this Chapter the measured data will be presented including the cuts applied to guarantee for their quality. First the measured muon lateral distributions are compared with simulated events and with the lateral distribution function used in reconstruction. Furthermore the measured muon size spectrum is shown for two zenith angle ranges and is compared to measurements of the KASCADE experiment.

5.1 The Data Sample

The data considered in the following study was collected from March 4, 2004 until March 22, 2006. The effective time of data taking of the Grande array was 370.4 days, the time in which both the Grande array and the KASCADE array were operating amounts to 362.8 days. Since the KASCADE array is essential to reconstruct the muon component of air showers, the latter time is relevant for the following discussions. In this time approximately 15.1 million events have been registered by the Grande array. In order to be considered a successfully measured and reconstructed event, several criteria have to be fulfilled:

- The reconstruction has to be successful on the third level.
- None of the 12 outer clusters of the KASCADE array, that are equipped with muon detectors, was missing.
- A minimum of 20 stations for the Grande array measured an energy deposit.
- The reconstructed shower core lies within a fiducial defined by a circle with 250 m radius around the center of the Grande array. This is to reduce the effect of misreconstructed cores at the border of the array, especially from showers originally outside the Grande array.

- The age parameter of the lateral distribution that describes the measured electron density distribution lies in the range of 0.4–1.4. This ensures the precision of the reconstructed electron size, especially close to the trigger threshold.

Part of this study was dedicated to inquire about the source of fake events in the KASCADE-Grande detectors, which has been found out to be connected to the nearby synchrotron facility ANKA. As a result, the following quality requirement has been added:

- The quality of data was not affected by artificial events caused by ANKA. This is controlled by a combination of characteristic event pattern and a data base containing information of activity at ANKA.

After requiring these cuts a total of $6.50 \cdot 10^4$ and $4.67 \cdot 10^4$ events remain, for zenith angles 0°–18° and 18°–25° respectively.

5.2 The Muon Lateral Distribution

In this section the measured muon lateral distributions are compared with simulations and their description by the used lateral distribution function is discussed.
The measured showers are binned in intervals of estimated energy, determined by a linear combination of electron and muon sizes given by

$$\log_{10}(E_{est}/GeV) = 0.313 \cdot \log_{10} N_e + 0.666 \cdot \log_{10} N_\mu + 1.24/\cos\theta + 0.580. \quad (5.1)$$

It is obtained by means of a linear regression analysis based on CORSIKA showers for five different primaries [29]. Furthermore the measured lateral distributions are shown in Fig. 5.1,Fig. 5.2, and Fig. 5.3 for three different zenith angle ranges, namely 0°–18°, 18°–25° and 25°–30°. These correspond approximately to an increase of traversed atmosphere by a factor of 1, 1.05, and 1.1 respectively.
Since each measurement contributes over a radial range of 280 m, and the distance distribution is not homogeneous, it is not easy to measure the whole lateral distribution over 600 m. For energies higher than 2×10^{17} eV the measured number of events is up to now too small to measure the muon lateral distribution over the whole range from 40 m to 700 m. The drawn lines correspond to equation 4.3 used in the reconstruction with the muon number N_μ set to the measured mean muon number in each interval.
For the first two energy intervals in all three zenith angles ranges the data is very well described by the used lateral distribution function. At higher energies and at radii smaller than 200 m the data is around 10% higher than the used function would expect. This effect is strongest in the first zenith angle range and decreases for higher zenith angle ranges. The highest energy interval of 8×10^{16} eV–1.6×10^{17} eV is characterized for radii larger than 500 m a 10% – 20% lower measured muon densities

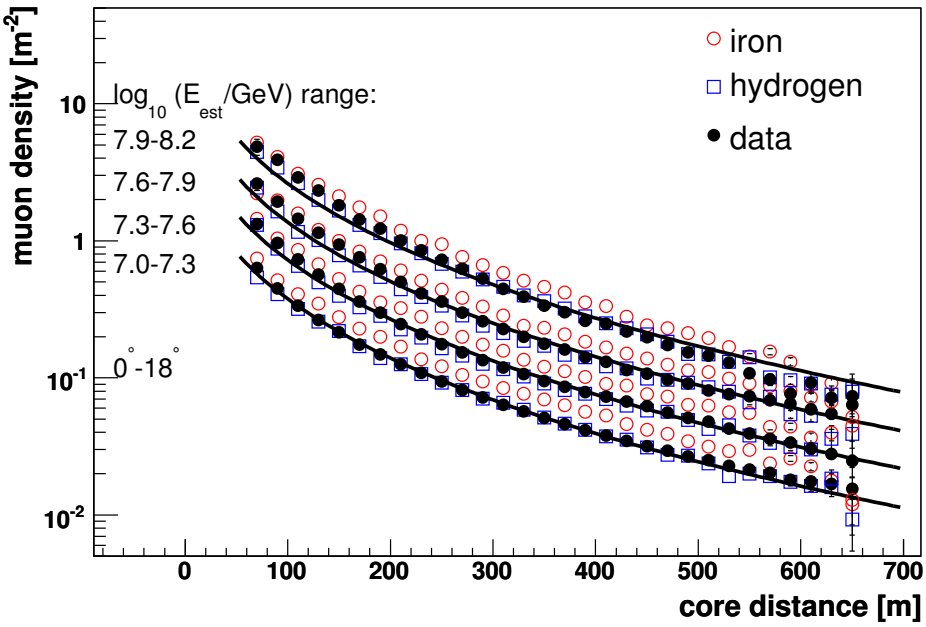

Figure 5.1: Measured muon density distribution for zenith angles 0°–18° and four estimated energy intervals. The lateral distribution function 4.3 with the muon number N_μ set to the measured mean muon number in each interval is shown.

than described by the function. For all energy and zenith angle intervals the measured muon densities agree with the simulations since they lie well between the hydrogen and iron predictions. Hydrogen induced air showers have a smaller muon size than iron induced air shower and therefore lower muon densities. The measured muon densities lie in general much closer to the hydrogen prediction than to the iron prediction.
In conclusion it is difficult to make a statement about a possible change of composition with increasing energy, based on the shape of the measured muon lateral distributions. This is mainly due to a limited sensitive area and limited radial range in which the muon densities are sampled. Further restrictions are introduced by limited detector resolution and reconstruction resolution.

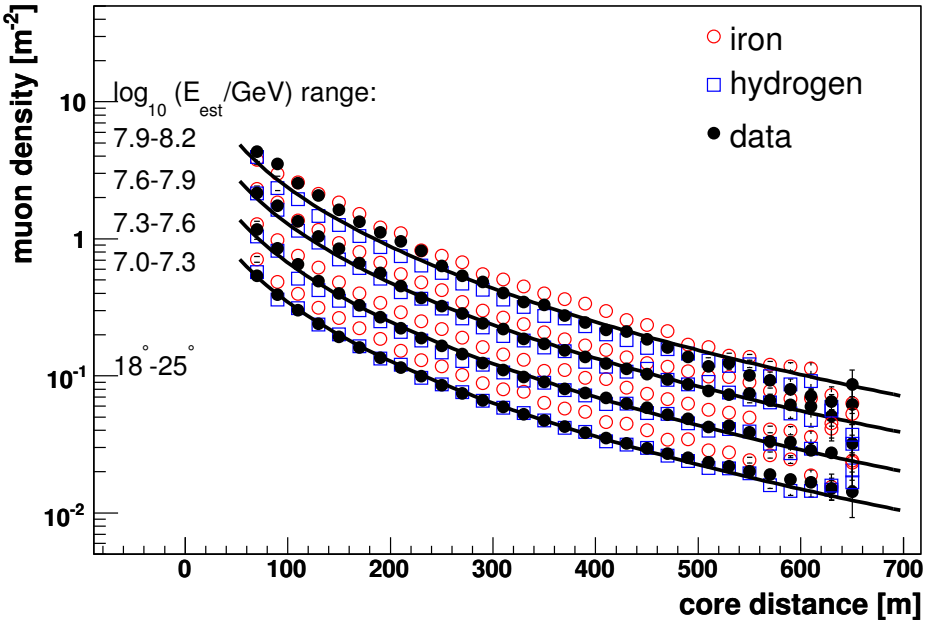

Figure 5.2: Measured muon density distribution for zenith angles 18°–25° and four estimated energy intervals. The lateral distribution function 4.3 with the muon number N_μ set to the measured mean muon number in each interval is shown.

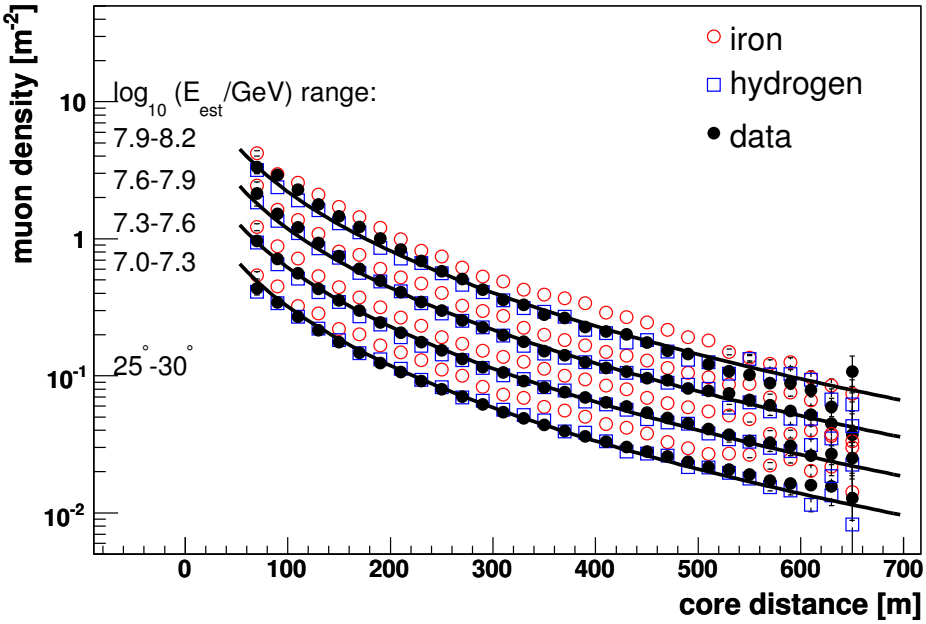

Figure 5.3: Measured muon density distribution for zenith angles 25°–30° and four estimated energy intervals. The lateral distribution function 4.3 with the muon number N_μ set to the measured mean muon number in each interval is shown.

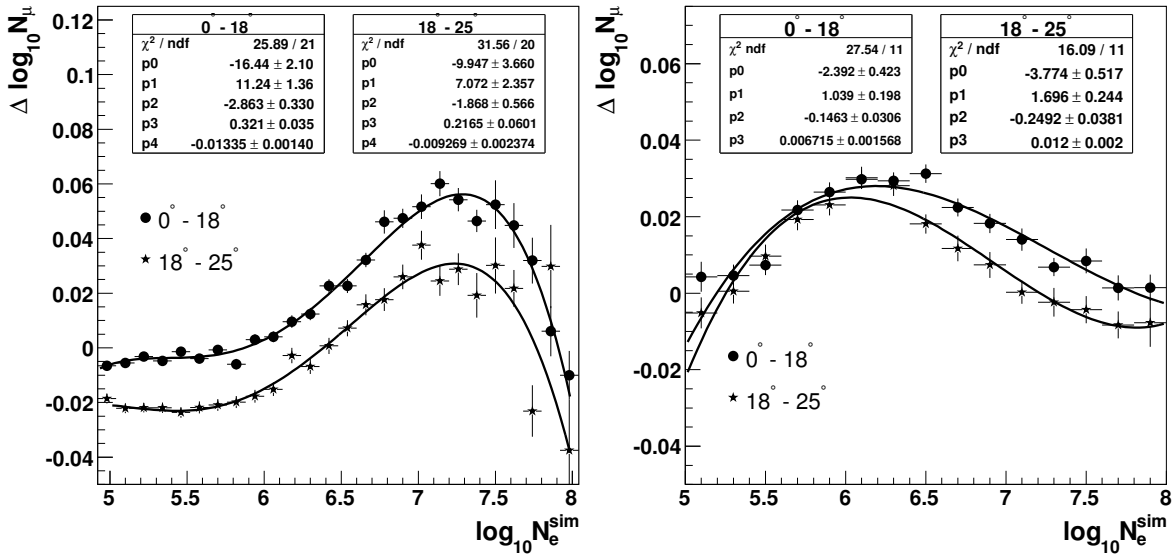

Figure 5.4: Average correction $\Delta \log_{10} N_\mu = \log_{10} N_\mu^{rec.} - \log_{10} N_\mu^{sim.}$ as function of electron number for hydrogen and iron air showers and for zenith angle ranges 0°–18° and 18°–25°. The functions used for KASCADE (left) and KASCADE-Grande (right) are shown.

5.3 The Spectrum of the Muon Size

The measured muon size spectrum of KASCADE-Grande is compared with the muon size spectrum measured by KASCADE. The KASCADE data was taken in an effective time of approximately 1300 days and standard quality cuts for the reconstruction were applied. These include a successful reconstruction, a minimum trigger condition, a shower age in the range of 0.2 to 2.1 (for a different NKG-function than equation 4.1), and a reconstructed shower core within 91 m distance to the center of the KASCADE array. Both muon size spectra are corrected for their systematic errors $\Delta \log_{10} N_\mu = \log_{10} N_\mu^{rec.} - \log_{10} N_\mu^{sim.}$ which are displayed in Figure 5.4 as function of the electron number $\log_{10} N_e^{sim.}$, with averaged values of hydrogen and iron initiated showers. The correction functions used are polynomials of third and fourth order for KASCADE and KASCADE-Grande respectively. Using $\log_{10} N_e^{sim.}$ as variable makes it less depending on the primary as using $\log_{10} N_\mu^{sim.}$ would be.
The spectrum measured by KASCADE presents a steepening of the spectrum in the first zenith angle range at a muon number of around $\log_{10} N_\mu = 4.7$. Due to attenuation the steepening in the second zenith angle range can be seen at a lower muon number $\log_{10} N_\mu \approx 4.6$. This steepening in the muon size spectrum corresponds to the knee of the light component in the primary energy spectrum. At a muon number of $\log_{10} N_\mu = 5.1$ and $\log_{10} N_\mu = 5$ respectively, one observes a flattening of the measured spectrum which is understood as a relative increase of the heavy component.

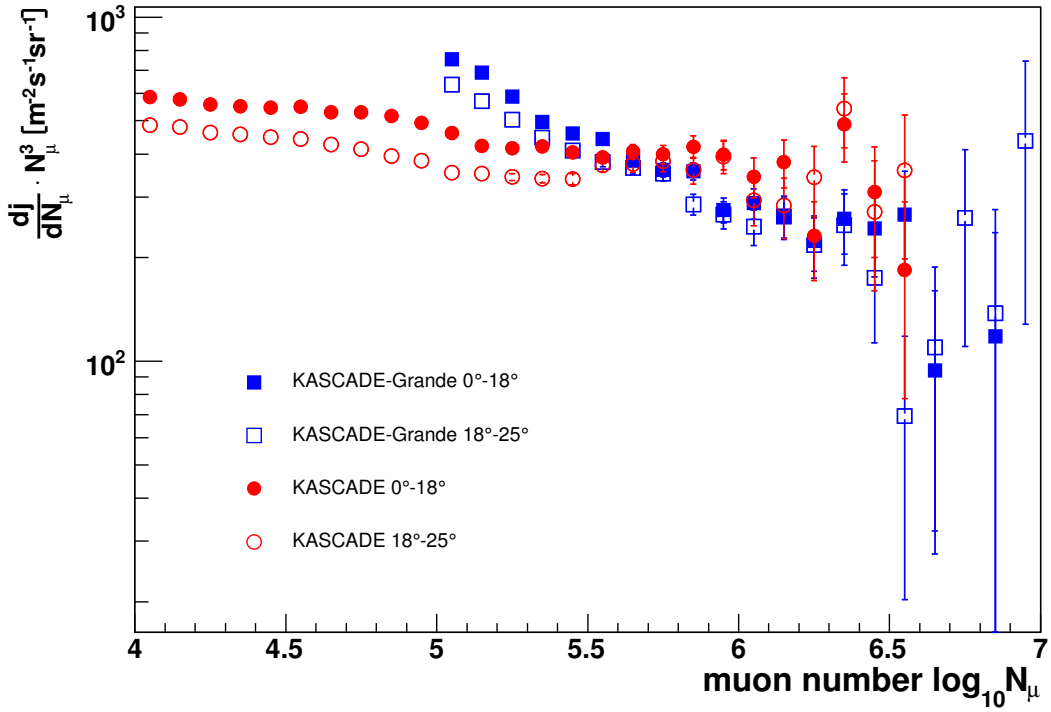

Figure 5.5: Comparison of muon size spectra measured by KASCADE and KASCADE-Grande for two zenith angle ranges. To clarify the structure the flux values are multiplied with N_μ^3.

The muon size spectrum measured by KASCADE-Grande is characterized by a higher flux than measured by KASCADE for muon numbers between $\log_{10} N_\mu = 5$ and $\log_{10} N_\mu = 5.5$. At threshold of 100% efficiency given by $\log_{10} N_\mu = 5$ the flux is estimated around 60% higher. The overestimate decreases for higher muon numbers. This can be understood by considering the spread of $\Delta \log_{10} N_\mu$ as it was indicated in Figure 4.5. For $\log_{10} N_\mu = 4.5$ the statistical uncertainty is around 80%, and reconstruction efficiency is around 20% to 60% for iron and hydrogen respectively (see Fig. 4.7). Even with a reduced efficiency these small events will cause an overestimate due to the steeply falling primary cosmic ray spectrum.
A possibility to take these effects into account are unfolding methods, that enable the comparison of observables from different experiments. In the following Chapter a method to unfold the muon size spectrum measured with KASCADE-Grande is discussed.

Chapter 6

Unfolding the Muon Size Spectrum

In the previous chapter was observed that a direct comparison of the muon size spectra measured by KASCADE and KASCADE-Grande is difficult. Reconstruction resolutions and systematic effects are different, changing the shape of the true size spectrum in different ways.
In general, often a physical interesting observable is not directly accessible, due to limited reconstruction resolution, efficiency effects etc. The measured distribution is obtained by a convolution of the true distribution with the instrumental response function. In order to correct on the smearing effects unfolding methods are applied, to obtain the quantity one is interested in.
In the case of air showers measured with the KASCADE experiment, the electron and muon sizes are used to reconstruct the energy spectra of single mass groups [11]. In order to compare the muon size spectrum measured by KASCADE-Grande with results from KASCADE, it will be unfolded to the original energy spectrum. In that case the response function does not only describe systematic effects of the apparatus like e.g. finite resolution but also the large intrinsic fluctuations in shower sizes of air showers of a given energy.
In this chapter a description of the problem to be solved by unfolding is given, the chosen method is explained and its precision is discussed in a comparison of Monte Carlo data sets.

6.1 Formulation of the Unfolding Problem

The "true" and physical relevant value $f(x)$ is related to the raw measured observable $g(y)$ by a convolution type integral, so-called *Fredholm integral* equation of 1st kind

$$g(y) = \int A(y,x) f(x) dx, \tag{6.1}$$

where A(y,x) is the response function, also known as *resolution* or *migration function.* The response function describes the instrumental answer to an event x and includes the instrumental resolution and efficiency.
Breaking the integral over x in equation 6.1 into a sum over j bins, it can be approximated as a matrix equation

$$y(i) = \sum_{j=1}^{M} A(i,j) \cdot x(j) = \sum_{j=1}^{M} A_{ij} \cdot x_j \qquad i = 1, \ldots, N \tag{6.2}$$

or

$$\overrightarrow{y} = \mathbf{A}\,\overrightarrow{x}. \tag{6.3}$$

N is the dimension of the measured data vector $\overrightarrow{y}$ and M is the dimension of the sought after true data vector $\overrightarrow{x}$, and $\mathbf{A}$ is the response matrix of dimension (N, M). In this analysis $\overrightarrow{y}$ corresponds to the muon size spectrum and $\overrightarrow{x}$ to the energy spectrum.

6.2 Solution Strategy

A solution of equation 6.2 is not standardly available and not guaranteed. The output vector $\overrightarrow{y}$ is affected by shower fluctuations and efficiency effects. The process of unfolding is strongly affected by these fluctuations and smearings. In general the response matrix is diagonally dominated and $\mathbf{A}$ is almost singular, as $\det(\mathbf{A}) \approx 0$. A direct inversion of this matrix is not possible, and would not provide a stable result since the solution would be affected by fluctuations in the data $\overrightarrow{y}$. In order to obtain a solution the method of regularization has to be included, i.e. the problem is replaced by an approximation whose solutions are much less sensitive to uncertainties in $\overrightarrow{y}$.
One possibility is to add a regularization function $S(\overrightarrow{x})$ weighted with a regularization parameter α. An estimate for the solution vector $\hat{\overrightarrow{x}}$ is characterized by a minimum for the χ^2 value given by

$$\chi^2 = \sum_{i=1}^{M} \frac{(y_i - \sum_{j=1}^{N} \mathbf{A}_{ij}\hat{x}_j)^2}{\sigma_i^2} + \alpha S((\overrightarrow{x}). \tag{6.4}$$

High values of α mean strong regularization and smoothing of the solution, for $\alpha \to \infty$ ignoring the data $\overrightarrow{y}$. With $\alpha \to 0$ no regularization would be achieved. A common method is the Tikhonov regularization [56, 47], that uses as measure of smoothness the value of the square of some derivative, typically the second, of the true distribution. A further method uses regularization functions based on entropy [51], where the entropy is interpreted as a measure of smoothness of the true distribution.
Other techniques are iterative methods of deconvolution, where one approaches the solution in a series of calculating steps. By choosing the stopping point of the iteration,

the solution is regularized. One of these methods is the Van Cittert [58] algorithm. Its general form to solve a linear discrete system is

$$\overrightarrow{x}^{k+1} = \overrightarrow{x}^{k} + \mu(\overrightarrow{y} - \mathbf{A}\overrightarrow{x}^{k}), \tag{6.5}$$

where k is the number of iterations, $\mathbf{A}$ is the system matrix and μ is the relaxation factor. To ensure convergence the relaxation factor μ has to be in the range of $0 < \mu < 2/\lambda_{max}$, where λ_{max} is the maximum eigenvalue of Matrix $\mathbf{A}$. The response matrix A is, as in this work, not necessarily a square matrix, with M unequal N. In that case one has to do the following replacements:

$$\overrightarrow{y'} = \mathbf{A^T}\overrightarrow{y} \quad \text{and} \quad \mathbf{A'} = (\mathbf{A^T A}). \tag{6.6}$$

One disadvantage of this algorithm is that one can obtain negative solutions, which would not be meaningful in this work of reconstructing the cosmic ray energy spectrum. The Gold algorithm [30] is an extension of Van Cittert's method, having the advantage that all components of its solution $\overrightarrow{x}$ are positive. Multiplying both sides of equation 6.3 with $\mathbf{A^T}$ gives

$$\mathbf{A^T}\overrightarrow{y} = \mathbf{A^T A}\overrightarrow{x}. \tag{6.7}$$

Matrix $(\mathbf{A^T A})$ is symmetric and therefore its eigenvalues will be real. The eigenvalues of matrix $(\mathbf{A^T A})(\mathbf{A^T A})$ are squares of these real eigenvalues, and thus must be positive. Equation 6.7 becomes

$$(\mathbf{A^T A A^T})\overrightarrow{y} = (\mathbf{A^T A A^T A})\overrightarrow{x}. \tag{6.8}$$

Using this in Eq. 6.5 the iterative algorithm then becomes

$$\overrightarrow{x}^{k+1} = \overrightarrow{x}^{k} + \mu(\overrightarrow{y}' - \mathbf{H}\overrightarrow{x}^{k}), \tag{6.9}$$

where matrix $\mathbf{H}$ is given by $(\mathbf{A^T A})(\mathbf{A^T A})$ and $\overrightarrow{y}' = (\mathbf{A^T A A^T})\overrightarrow{y}$. In the Gold algorithm one uses a local variable relaxation factor given by

$$\mu_i = \frac{x_i^k}{\sum_{j=1}^{N} \mathbf{H}_{ij} x_j^k}. \tag{6.10}$$

Using this relaxation factor in Eq. 6.9, one gets the Gold algorithm for the ith element of solution vector $\overrightarrow{x^{k+1}}$

$$x_i^{k+1} = \frac{y_i' x_i^k}{\sum_{j=1}^{N} \mathbf{H}_{ij} x_j^k}. \tag{6.11}$$

6.3 Determination of the Response Matrix

The elements of the response matrix contain the probabilities that a shower with a certain measured muon size $\log_{10} N_\mu^i$ originates from a cosmic ray particle of a certain energy $\log_{10} E^j$. So for the elements of the matrix for one primary applies

$$A_{ij} = P(\log_{10} N(i)_\mu | \log_{10} E(j)). \tag{6.12}$$

Actually for every chosen primary a sub-matrix is filled, thus equation 6.2 becomes

$$y_i = \sum_{l=1}^{l_{max}} \sum_{j=1}^{M} A_{ij}^l x_j^l \qquad i = 1, \ldots, N \tag{6.13}$$

with l_{max} the number of chosen primaries, in this case two. For this analysis hydrogen and iron were chosen as constituents of cosmic rays representing the light and heavy components.
The response matrix was determined using detailed simulations of cosmic rays events, i.e. air showers generated by CORSIKA [34] using the interaction models FLUKA [26] and QGSJET [37] were used as input for detailed simulations based on GEANT [18] of the KASCADE experiment. For each primary and zenith angle range approximately one million events were generated, following a E^{-2} spectrum in the energy range of 10^{15} – 10^{18} eV. As zenith angle ranges the two intervals from 0° – 18° and 18° – 25° were chosen. The response matrix does not depend on the true muon size of an air shower, it describes directly the relation between energy of the primary cosmic ray particle and the distribution of reconstructed muon sizes. It implicitly includes shower fluctuations in true shower size, systematic effects of reconstruction and efficiency.
The interval width in energy is chosen in such a way that the shape in the energy spectrum of E^{-2} in the simulations does not affect the value for an interval in the response matrix. The chosen bin width is 0.1 in logarithm of energy, which corresponds approximately to a factor of 1.25 from bin to bin. The mean values of the distributions of muon sizes differ for monoenergetic simulations only weakly from simulations following an energy spectrum of E^{-2}. The results of the analysis are compared with an analysis for which the response matrices were shifted by half a bin width in energy, to check for any effects on the shape of the energy spectrum.
The number of intervals in the muon size spectrum is chosen in a way that agrees with the reconstruction precision, i.e. not too small, and that contains enough information for the unfolding algorithm, so not too few and too large. Atmospheric effects on the measured muon size are smaller than the chosen bin widths and therefore neglected.
Figure 6.1 shows the muon number response distribution for the KASCADE-Grande experiment for various energies in two zenith angle ranges, $\theta < 18°$ (left), and $18° < \theta < 25°$ (right). One sees that for higher zenith angles the muon distribution is shifted by approximately $\Delta \log_{10} N_\mu = 0.05$ to the left. Furthermore one can see that iron

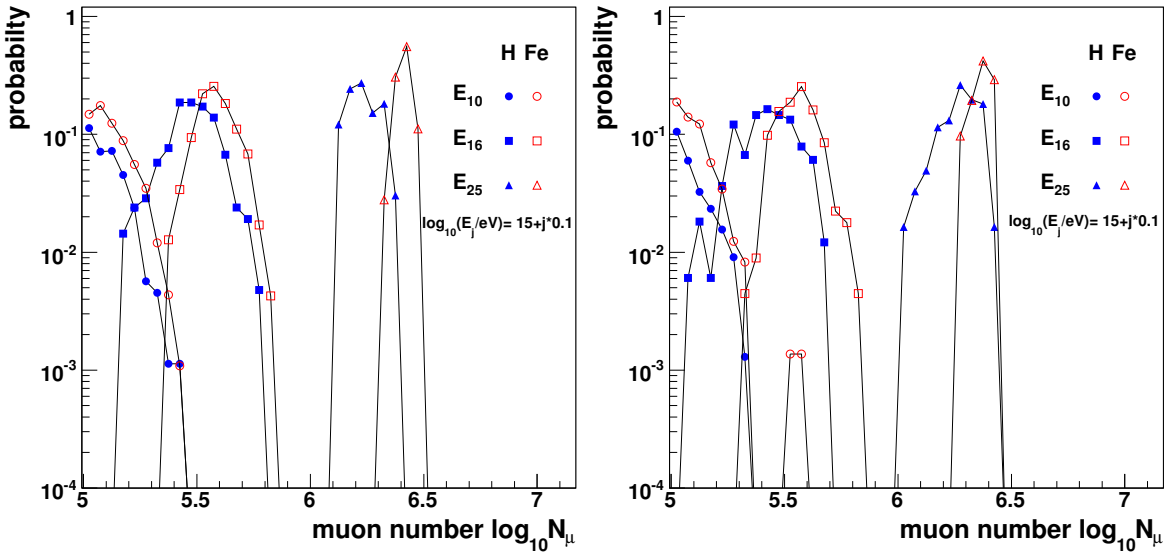

Figure 6.1: Muon number probability distributions for zenith angle $\theta < 18°$ left, and $18° < \theta < 25°$ right. The distributions for hydrogen and iron induced air showers of $8.9 \cdot 10^{15}$ eV, $3.5 \cdot 10^{16}$ eV, and $2.8 \cdot 10^{17}$ eV are represented.

induced showers have a narrower distribution than hydrogen induced ones and that with increasing energy the distribution of both primaries grows narrower. A complete overview of the elements of the response matrices for both zenith angle ranges and for iron and hydrogen primaries is given in Appendix A.1.
In order to investigate for possible systematic effects that could influence the regularization parameter, several Monte Carlo data sets have been created. The generated spectra comprise various combinations of knee positions for hydrogen and iron, also some non physically motivated, in order to study the stopping criterion and later the sensitivity to the composition. Their characteristics are listed in Table 6.1.

6.4 Stopping Criterion of Iteration

The precision of the analysis is discussed using simulations. With the simulations an energy spectrum can be composed and the reconstructed energy spectrum is compared to the true original one, enabling to understand systematic effects. Furthermore the muon size spectrum can be used to generate randomly new input vectors from the original one, allowing to study statistical effects of the used method. An important point in the used Gold unfolding method is when to stop the iterative procedure. At the beginning the estimated solution is far off from the truth, beyond a certain point

Set	Element	knee position	γ_1	γ_2
Set1	hydrogen	10^{16} eV	2.0	2.5
	iron	10^{17} eV	2.0	3.0
Set2	hydrogen	10^{17} eV	2.0	2.5
	iron	10^{16} eV	2.0	2.5
Set3	hydrogen	-	2.0	-
	iron	10^{17} eV	2.0	2.7
Set4	hydrogen	-	2.0	-
	iron	-	2.0	-

Table 6.1: Characteristics of generated energy spectra.

the estimated solution will describe the measured shower size spectrum including its statistical fluctuations and not represent the "true" cosmic ray spectrum anymore. In the following it will be discussed how to find that certain point to stop the iteration. An obvious quantity to characterize the stopping point of the iterative solution is the chi-square value. It is obtained by comparing the input vector $\overrightarrow{y}$ with the folded solution $\overrightarrow{x}_k$ for every iteration step k

$$\chi^2_k = \frac{1}{M} \sum_{i=1}^{M} \frac{(y_i - \sum_{j=1}^{N} \mathbf{A}_{ij} x_j^k)^2}{y_i}. \tag{6.14}$$

Figure 6.2 left shows the development of χ^2 with the number of iterations for simulations. One sees a steep decrease for the first iteration steps and then a continuous slow decrease for higher iteration numbers. This is also apparent from Figure 6.2 right, where $\Delta\chi^2$, the difference in χ^2 of successive iteration steps, in dependency of the iteration number is displayed. The error bars indicate the spread of the $\Delta\chi^2$ values obtained at a fix number of iteration steps. They are obtained by creating 100 data sets based on one original data set and comparing the results of each unfolding. One observes that especially at higher iteration numbers the $\Delta\chi^2$ shows a large spread. In order to be independent from possible differences between the used Monte Carlo test samples and the data sample, as stopping point a certain value of $\Delta\chi^2$ is chosen instead of an absolute iteration step number.

The optimal stopping point is characterized by a minimum of the Weighted Mean Square Error (WMSE), that has contributions from statistical uncertainties and systematic errors. With higher iteration levels the systematic errors decrease and statistical uncertainties increase, generating a minimum in the total WMSE. The weighted

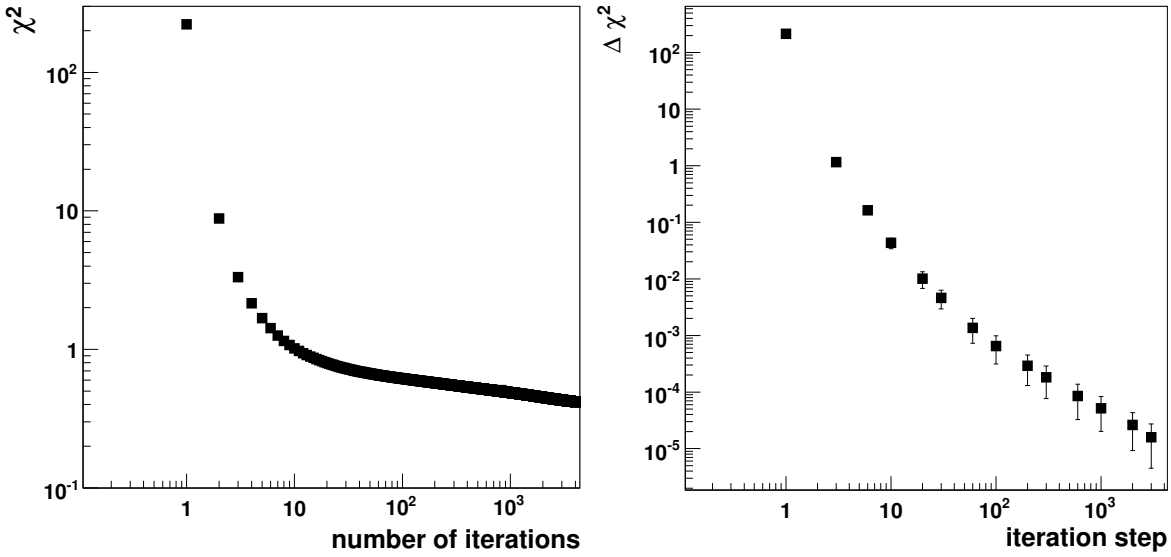

Figure 6.2: χ^2 and $\Delta\chi^2$ values for different number of iterations for a set of simulated data.

mean square error is given by

$$WMSE = \frac{1}{M}\sum_{i=1}^{M}\frac{\sigma_i^2 + b_i^2}{x_i}, \tag{6.15}$$

with the variance σ_i^2 and the biases b_i of the estimated solution vector.

6.4.1 Statistical Uncertainty

In order to estimate the statistical uncertainty of the estimated solution, L=100 sets of muon size spectra are created with Monte Carlo methods from the original data set. Consequently the variance of the solution vector depending on iteration level k, characterized by $\Delta\chi^2$, as well as the variance of the solution at a certain energy and for a given iteration level can be calculated. The weighted mean variance is given by

$$\Delta_{stat} = \frac{1}{M}\sum_{i=1}^{M}\frac{\overline{x_i^2} - \overline{x}_i^2}{x_i}, \qquad \text{with } \overline{x}_i = \frac{1}{L}\sum_{l=1}^{L} x_i^l \tag{6.16}$$

with M the dimension of the solution vector and L the number of data sets used. Figure 6.3 left presents the weighted mean variance as function of iteration level $\Delta\chi^2$. For the contribution of weighted mean variance one sees an increase for higher iteration levels characterized by small $\Delta\chi^2$-values. At the beginning the solutions are similar

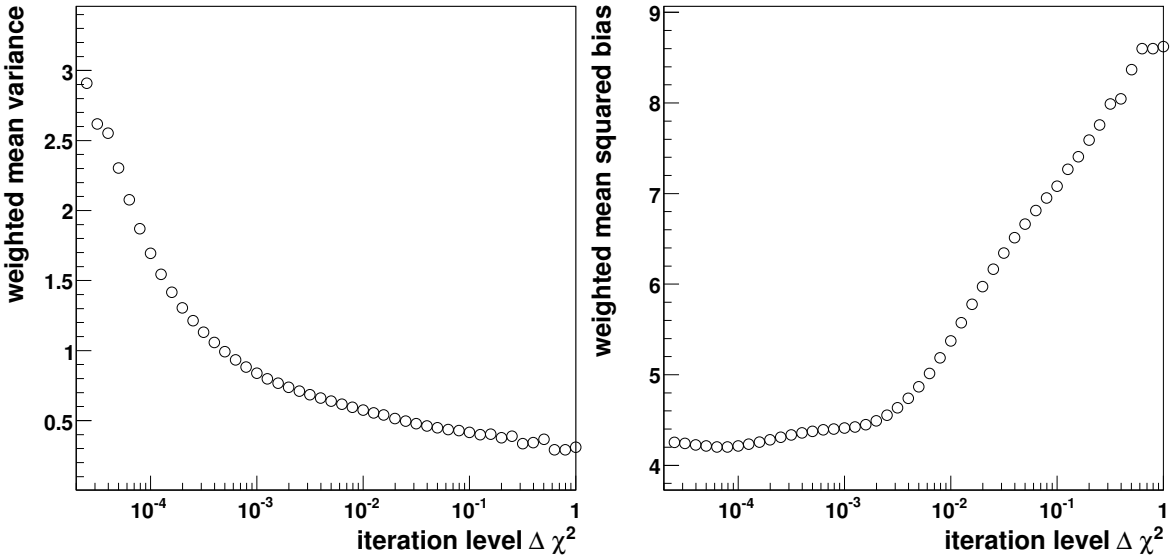

Figure 6.3: Statistical uncertainty (left) and systematic error (right) depending on iteration level $\Delta\chi^2$.

due to identical starting points and they describe the general shape of the solution. From $\Delta\chi^2$-values $<\approx 10^{-3}$ on, one sees a strong increase of the weighted mean variance towards smaller $\Delta\chi^2$ values.

6.4.2 Systematic Error

For the used simulated spectrum the true energy spectrum is known and can be compared to the reconstructed one. The weighted mean squared bias is given by

$$\Delta_{sys} = \frac{1}{M}\sum_{i=1}^{M}\frac{b_i^2}{x_i^{\mathrm{MC}}} = \frac{1}{M}\sum_{i=1}^{M}\frac{\frac{1}{L}\sum_{l=1}^{L}(x_i^l - x_i^{\mathrm{MC}})^2}{x_i^{\mathrm{MC}}}. \tag{6.17}$$

On the right hand side in Figure 6.3 the weighted mean squared bias is shown. A clear decrease with increasing iteration level is visible. For $\Delta\chi^2$-values $\approx 2\cdot 10^{-3}$ the dependency flattens and further iterations do not yield a large improvement of the systematic effects. In Figure 6.4 the total weighted mean square error is shown, as sum of the contributions in Fig. 6.3 left and right. There is a clear minimum visible at $\Delta\chi^2 \approx 2\cdot 10^{-3}$, corresponding to the optimal stopping point of the iterative process.

To study if the stopping criterion is sensitive to the used data sample, its behavior for various Monte Carlo energy spectra is studied. The generated spectra comprise various combinations of knee positions for hydrogen and iron as listed in Table 6.1.

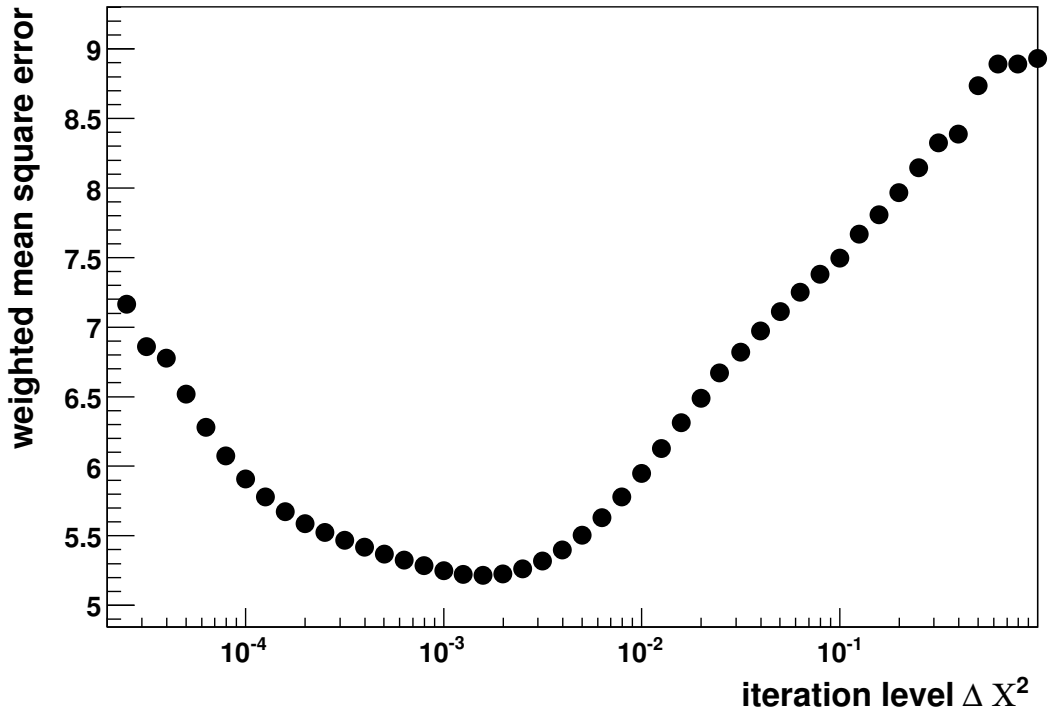

Figure 6.4: Total weighted mean square error depending on iteration quality $\Delta\chi^2$.

The resulting distributions of WMSE are included in Appendix A.2, there is no strong sensitivity of the stopping criterion on the chosen composition. They all indicate the presence of a clear minimum in the range of $\Delta\chi^2 \approx 2 \cdot 10^{-3}$.

6.4.3 Weighted Sum of Squares

An alternative way to determine the regularization parameter, in this case the stop criterion characterized by a $\Delta\chi^2$ value, is to look at the biases and their variances. One can construct the weighted sum of squares, given by

$$\chi_b^2 = \frac{1}{M} \sum_{i=1}^{M} \frac{b_i^2}{s_{b,i}^2}, \tag{6.18}$$

where b_i are the biases of the estimated solution vector as in equation 6.17 and $s_{b,i}^2$ their variances. The bias decreases for higher iterations. The ideas is, that at the stopping point the standard deviations of the biases are approximately equal to the biases themselves. A further reduction of the bias would not improve the solution, since it would introduce as much error as it removes. The stop criterion then is a value of χ_b^2 close to one. In Figure 6.5 an overview of the χ_b^2 values as function of

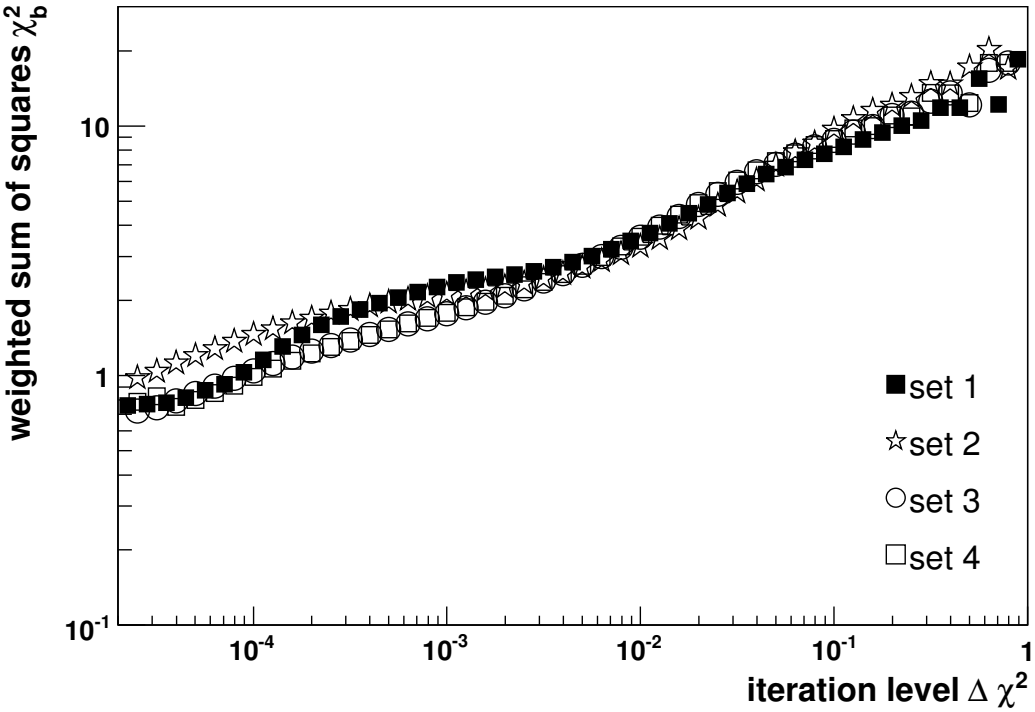

Figure 6.5: Weighted sum of squares χ^2_b as function of iteration level $\Delta\chi^2$ for various simulation sets.

$\Delta\chi^2$ for the different simulation sets is given. For all of them one can see a continuous decrease with iteration numbers. The condition χ^2_b is reached at iteration levels of $\Delta\chi^2 \approx 2 \cdot 10^{-4}$. At the previously determined value $\Delta\chi^2 \approx 2 \cdot 10^{-3}$, the χ^2_b is smaller than or around two. Together with the large and flat minimum in WMSE one does not see large differences between the solutions at these two iteration levels.

6.5 Sensitivity to Composition

Since the mean values between the muon distribution of iron and hydrogen induced air showers differ by $\Delta \log_{10} N_\mu = 0.15$, which corresponds to 3 bins, a sensitivity of the one dimensional unfolding to the primaries is not obvious. In order to check if the one dimensional unfolding of the muon size spectrum is sensitive to a possible change of the composition, the results are compared to the true input spectra for several simulated energy spectra with different assumed compositions as described in Table 6.1. The results are not characterized by a very high sensitivity to the composition. For some chosen input spectra the composition is reconstructed well (e.g. set 3 and 4 in Figure 6.6), though this might be due to a systematic effect of the method. The

solutions always propose a slightly hydrogen dominated composition, even if the chosen simulated input spectra had only a weak contribution from hydrogen. This can be seen for simulation set 1 in Figure 6.6, where the reconstructed hydrogen flux is reconstructed a factor 2–3 too high, and the iron flux accordingly too low. This effect does not seem to be correlated with the number of entries in a given energy bin, since for set 1 it differs over the whole range, also for bins with more than 100 events. Sets 3 and 4 present deviations up to a factor of 1.5, but agree reasonably well with the original spectra. The total spectrum is in all four cases well reconstructed, which can be seen in Figure 6.7. It shows the ratio of reconstructed and original energy spectrum as function of energy. The flux in the first energy bin is for all sets around 30% too high, which is due to being at the threshold of 100% efficiency. Further discrepancies range mostly in the range of 20%, larger biases are visible at high energies in set one and two that are due to lower number of events in corresponding energy bins. A separate estimate of systematic biases as function of number of entries is given is chapter 7.1 with the analysis of the measured data.

Since the unfolding exhibits only a limited sensitivity to the chosen composition, also unfolding with assuming only one component is considered to give an upper and lower estimate for the solution. Figure 6.8 shows the WMSE as function of iteration depth $\Delta\chi^2$ for pure hydrogen and pure iron assumption, using as input spectrum set 1 with a mixed composition. In contrary to Fig. 6.4, both assumptions do not lead to a clear minimum in WMSE. The pure hydrogen assumption shows a weak minimum at $\Delta\chi^2 \approx 0.1$, but the mean squared bias increases for higher iteration depths instead of decreasing. Furthermore the value of WMSE is higher than for an assumption of mixed composition. The pure iron assumption does not present a minimum in the WMSE distribution, instead the mean squared bias increases with ongoing iteration.
One can conclude that the unfolding needs two components. The spread of muon size distributions of hydrogen are too large to describe a measured muon size spectrum satisfactorily. For the iron instead the muon distributions are too narrow to describe the whole measured muon size distribution.
The considerations done so far apply for zenith angles $\theta < 18°$. Also for the second zenith angle interval 18°–25° the stop criterion has been determined. Due to different response matrices for this zenith angle range, the optimal stopping point differs slightly from the one obtained for 0°–18°. Figure 6.9 shows that $\Delta\chi^2 \approx 6 \cdot 10^{-4}$ is an optimal stopping point. As expected also here the stopping criterion is nearly independent of the used simulated input spectrum.

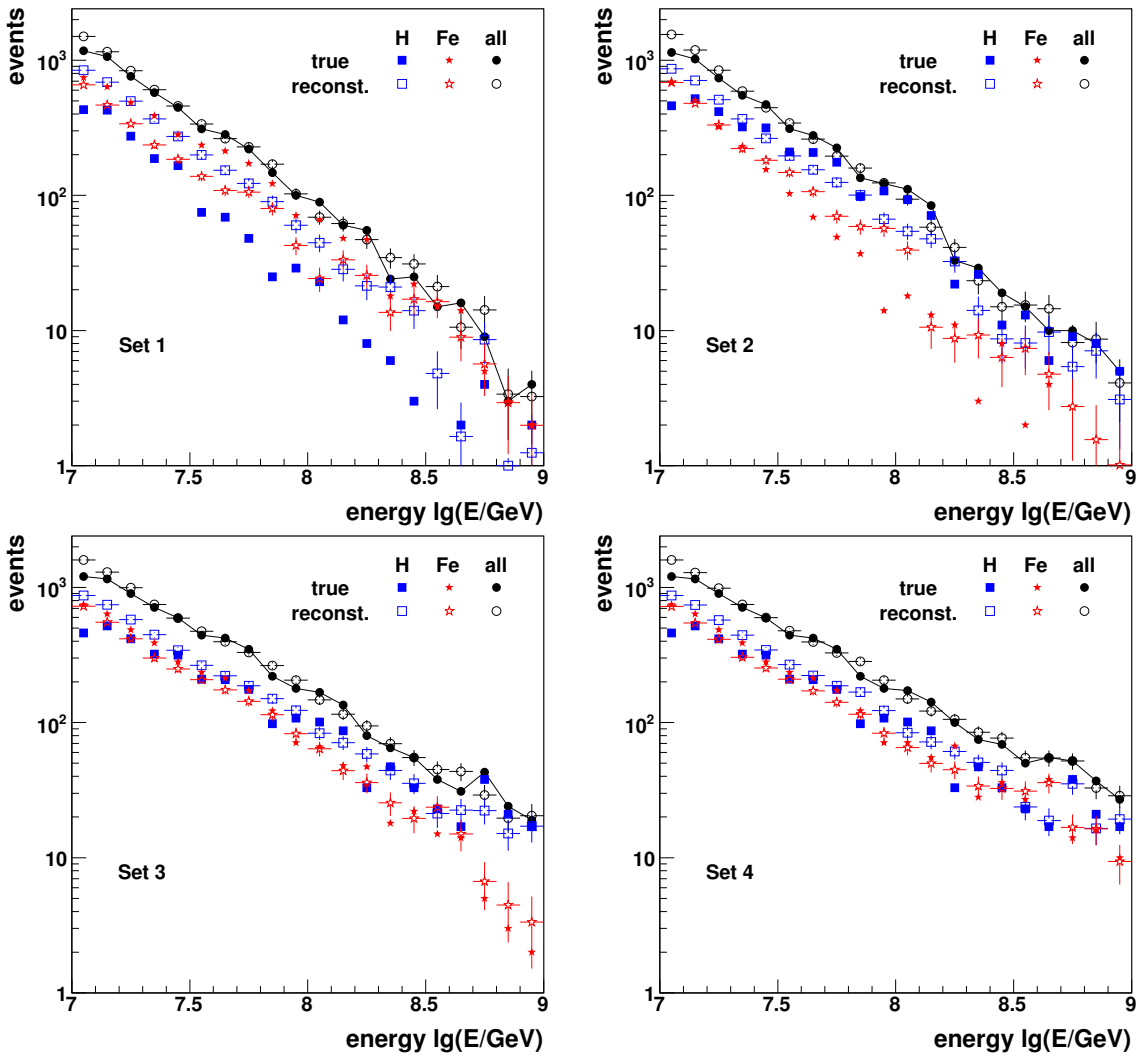

Figure 6.6: Unfolding results of different simulation sets according to Table 6.1. The true and reconstructed values for the components hydrogen and iron and their sums are shown.

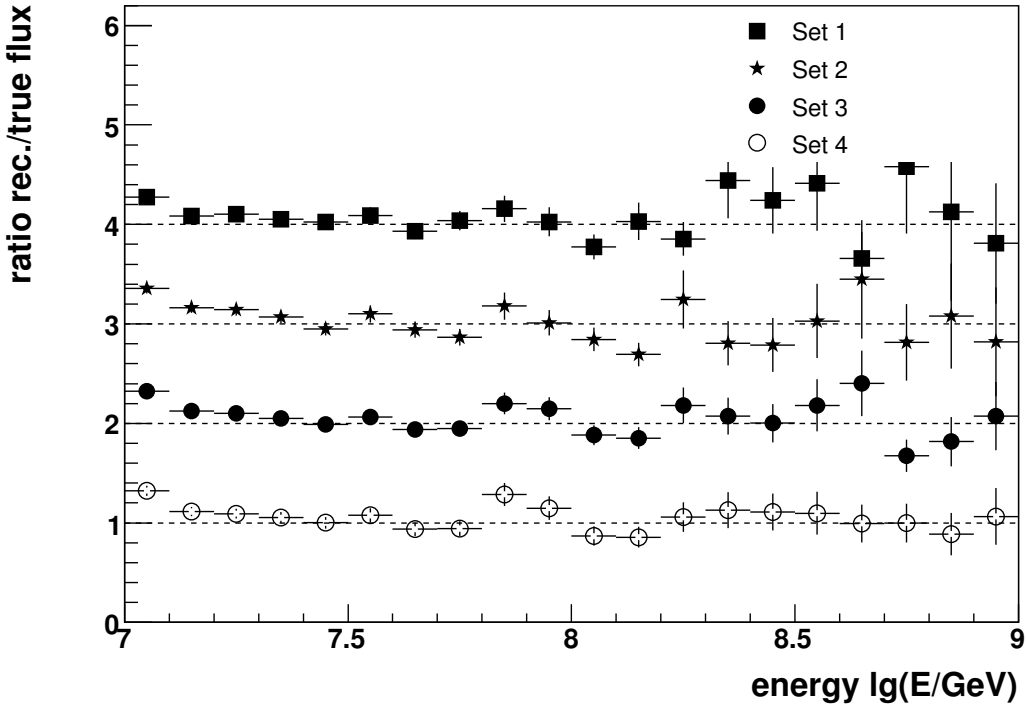

Figure 6.7: Comparison of reconstructed and true fluxes for various simulation sets. The ratios reconstructed divided by true flux, are plotted with an offset for clarity reasons. The dashed lines indicate a ratio of one respectively.

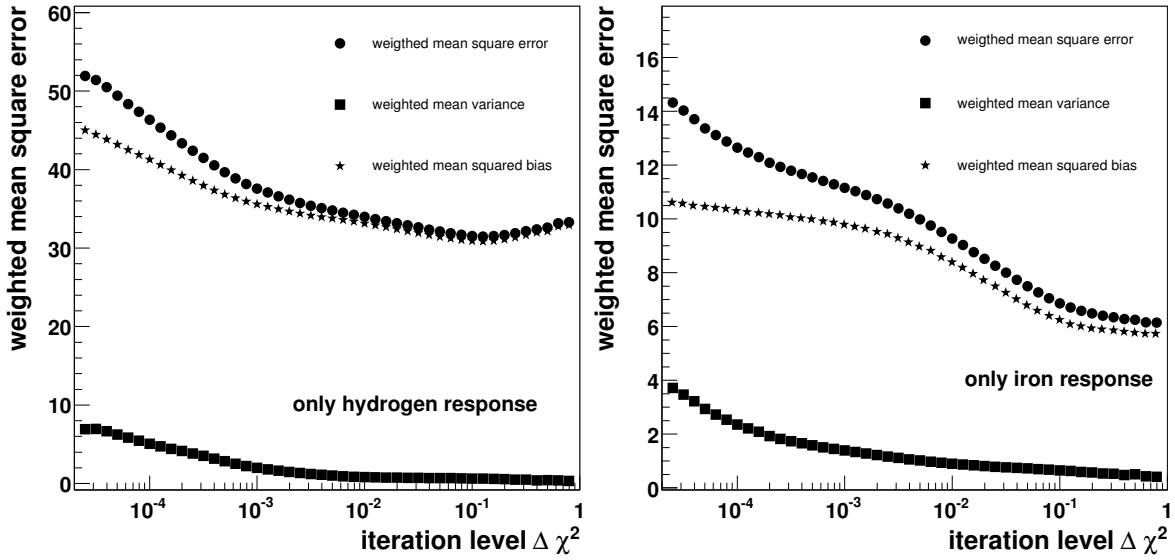

Figure 6.8: Weighted mean square error for assuming only hydrogen response matrix (left) and only iron response (right) during unfolding of set 1.

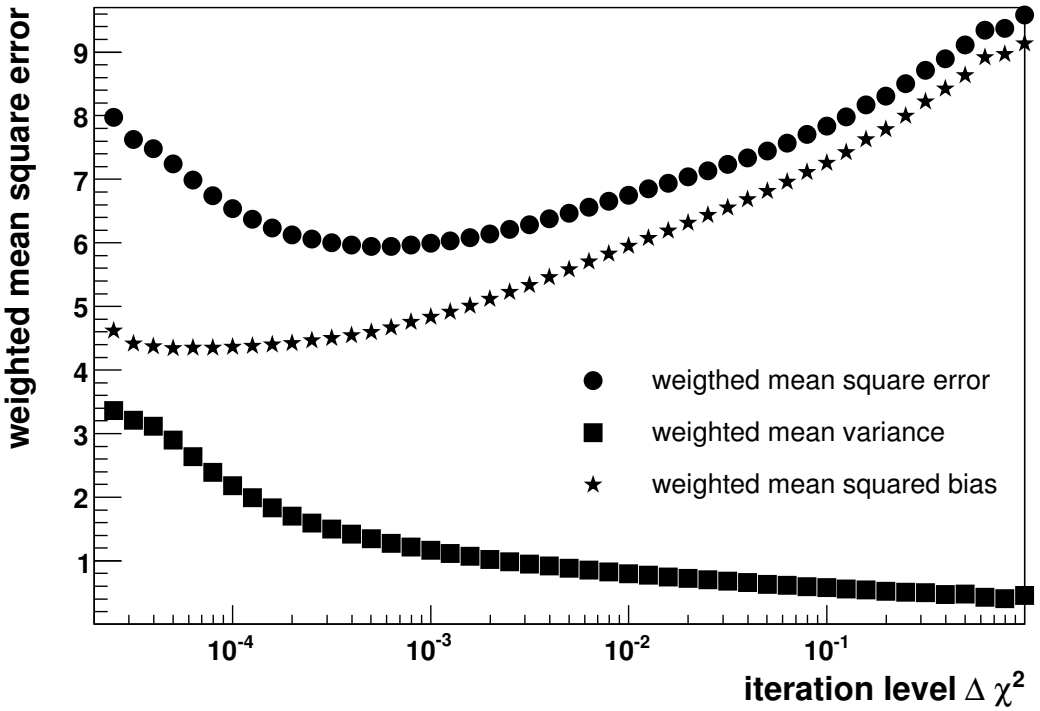

Figure 6.9: Weighted mean square error depending on iteration level $\Delta\chi^2$ for zenith angles 18°–25°.

Chapter 7

Analysis of Muon Size Spectrum

In this chapter the measured muon size spectrum is analyzed with the previously described unfolding method. The precision of the results is discussed and a comparison to previous results of KASCADE is presented.

7.1 Discussion of Errors

There is only one set of measured data, which is itself a sample generated by the true flux of particles hitting the earth.The statistical uncertainty of the data set was studied by using the same method as in Chapter 6.4.1. The measured muon data is used as a sample to create new muon data sets that are each unfolded. By comparing the results of the various unfoldings one can estimate the statistical uncertainty of the used method in this analysis. The statistical uncertainty σ_i for a given energy bin i is given by

$$\sigma_i^2 = \frac{1}{L}\sum_{l=1}^{L}(x_{i,l} - \overline{x}_i)^2 \tag{7.1}$$

where L is the number of data sets created. In Figure 7.1 (left) the relative statistical uncertainty is shown as function of primary energy. For energies lower than 10^{16} eV, which corresponds to being below 100% efficiency, an increase in fluctuations can be observed. For energies above threshold the relative statistical uncertainty is around 10%, though the reconstructed fluxes based on unfolding of simulation set 1 have larger fluctuations. This is due to lower entry numbers in that set compared to other considered simulation sets and the data set. This is displayed in Figure 7.1 (right), where the relative statistical uncertainty is shown as a function of number of entries in a given energy bin. In this Figure only entries above threshold are considered. One can see that for entry numbers of 100, the statistical uncertainty is around 10% and decreases with higher entry numbers. For values of ten entries the uncertainty is 60% to 70%, and one would expect an uncertainty of 100% at entry numbers of around six.

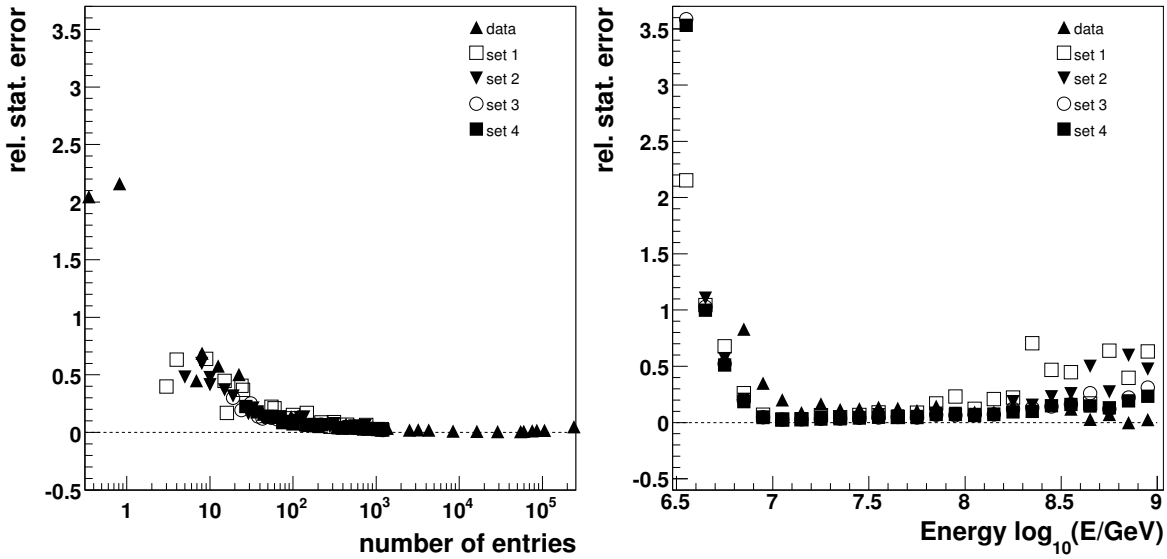

Figure 7.1: Relative statistical uncertainty for the total energy spectrum depending on primary energy (left) and number of entries in a given energy bin (right).

The main source for systematic errors is the limited statistics of simulations that were used to fill the response matrices, especially at highest energies.
Figure 7.2 (left) illustrates how the relative systematic bias depends on the number of entries. These bias were obtained with Monte Carlo studies where the true spectra were known. Simulation set 1, that has iron as a major component, is characterized by relatively large biases since the used unfolding method proposes always a slightly hydrogen dominated solutions. For number of entries higher than 30 a good agreement between the reconstructed and true spectra is seen. For smaller number of entries the systematic error can be up 70%. The dashed lines indicate a bias of 20%, that covers most of obtained biases. Therefore this value is used to obtain an estimate of the absolute systematic errors for the unfolded spectra.
Figure 7.2 (right) presents two results of unfolding the measured muon size spectrum for zenith angles 0°–18°. The filled symbols correspond to the results for the standard response matrices described in Chapter 6.3 and listed in A.1. The open symbols correspond to the results for an analysis with the response matrices shifted by half a bin width on the energy axis. This was done to check for any effects of the E^{-2} spectrum in the simulations that were used to fill the response matrices.
The obtained results agree very well and, with the used bin width of 0.1 in logarithm of energy, the shape of the energy spectrum in simulations does not have a significant effect.

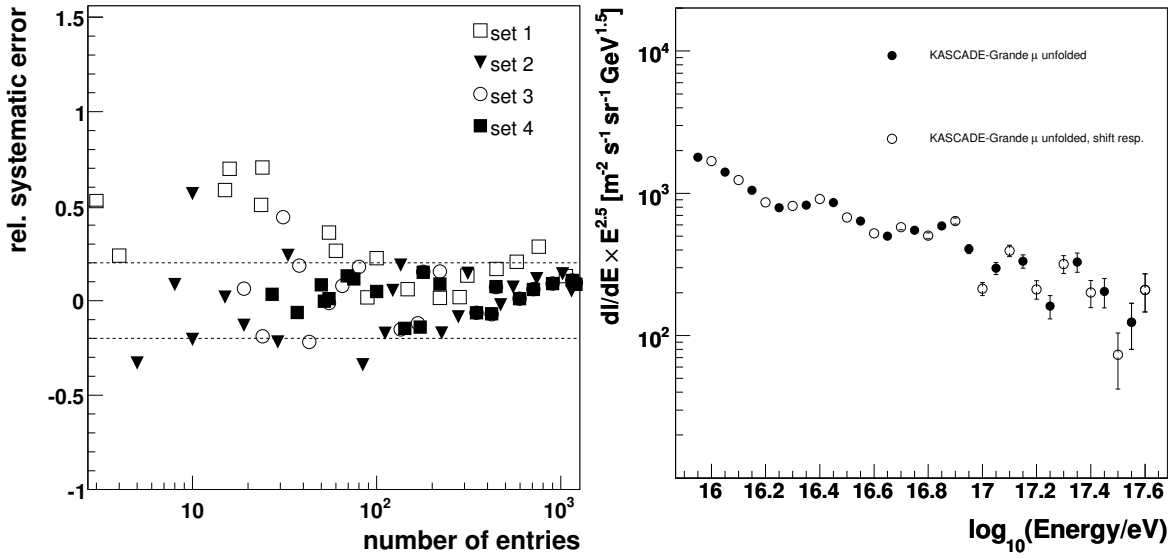

Figure 7.2: Left: Systematic bias of the total energy spectrum depending on number of entries. Right: Comparison of unfolding with shifted response matrices for 0°–18°.

7.2 Results

The results are obtained by unfolding the muon size spectrum with the Gold algorithm. In Fig. 7.3 and 7.4 the results of unfolding for the two zenith angle ranges 0°–18° and 18°–25° are shown. The error bars of the total spectrum indicate the total statistical error as squared sum of Poissonian statistics and uncertainties determined according to Figure 7.1. Even though the unfolding does not present a large sensitivity to the components, the hydrogen and iron contributions are indicated since they are both necessary to describe the measured muon size spectrum.
A comparison of the unfolded total energy spectrum for zenith angles 0°–18° with previous results from KASCADE, based also on the QGSjet assumption, is illustrated in Figure 7.5. A very good overlap in the energy range of 10^{16} eV to 10^{17} eV can be observed. The energy spectrum reaches up to an energy of 3×10^{17} eV and no knee is observed in that energy range. The error bars indicate the statistical uncertainty of the solution. The filled area represents the total error obtained by the sum in quadrature of the statistical and systematic errors. The systematic error is obtained according to the left part of Figure 7.2. Figure 7.6 displays the results for zenith angles 18°–25° with the statistical and total errors. A comparison with KASCADE results in this zenith angle range is not available and therefore not shown.
The quality of the solution can be characterized by the χ^2 value, which is obtained by folding the solution with the response matrix and comparing the resulting vector with the original data vector. For the first and second zenith angle ranges one obtains

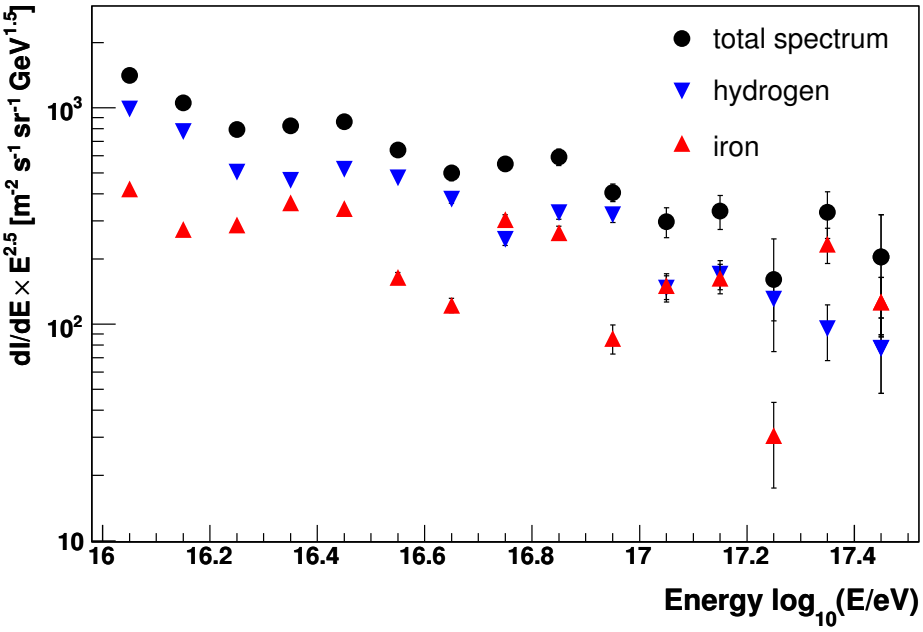

Figure 7.3: Unfolded energy spectra for first zenith angle interval 0°–18°. The reconstructed total spectrum and the spectra of hydrogen and iron are shown. The error bars indicate the total statistical uncertainty.

values of χ^2 per degree of freedom of 2.59 and 2.25 respectively. These values are not very satisfying considering the number of degrees of freedom $N_{\text{d.o.f.}} = 37$. Figure 7.7 indicates how much each bin of the muon size spectrum contributes to the total χ^2 value. One can see that the main contributions lie especially in the range of muon numbers smaller than $\log_{10} = 5.5$. This means that this region is not very well described by the solution, which is due to a not completely correct description of the muon size distribution at corresponding low energies. This can be due to a limited decription of shower fluctuations at these energies and more important to a not full description of the istrumental answer to events with threshold energies. At higher energies the measured data is well described by the estimated solution.

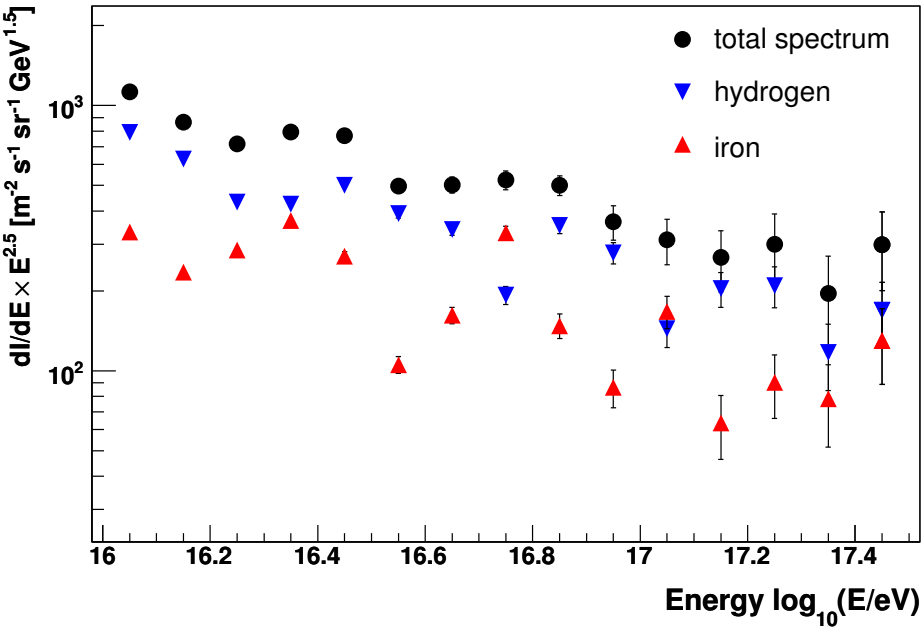

Figure 7.4: Unfolded energy spectra for second zenith angle interval 18°–25° . The reconstructed total spectrum and the spectra of hydrogen and iron are shown. The error bars indicate the total statistical uncertainty.

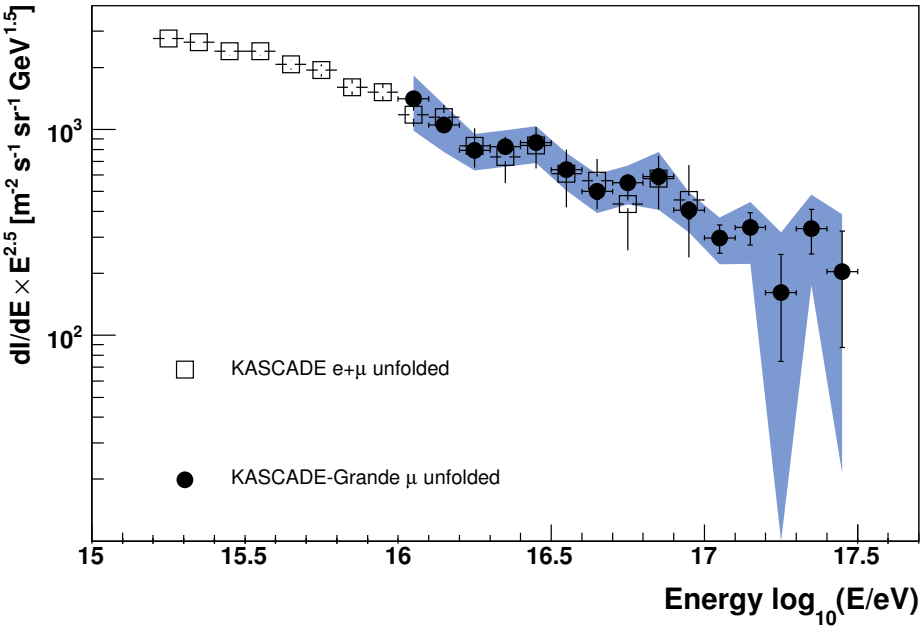

Figure 7.5: Unfolded total energy spectrum for zenith angle range 0°–18° compared to results of QGSjet assumption from [11]. Error bars indicate statistical error and the filled area represents the total error.

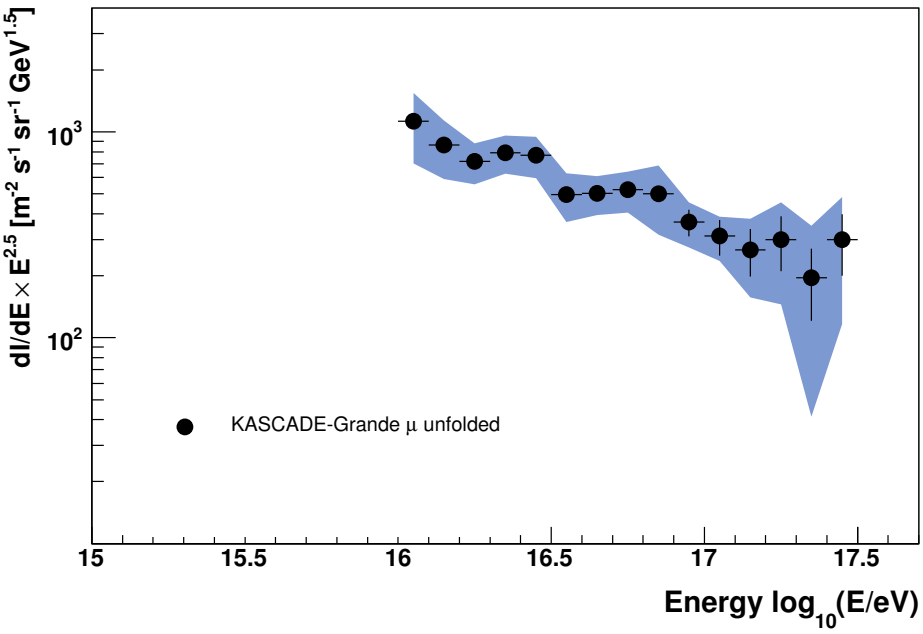

Figure 7.6: Unfolded total energy spectrum for zenith angle range 18°–25°. Error bars indicate statistical error and the filled area represents the total error.

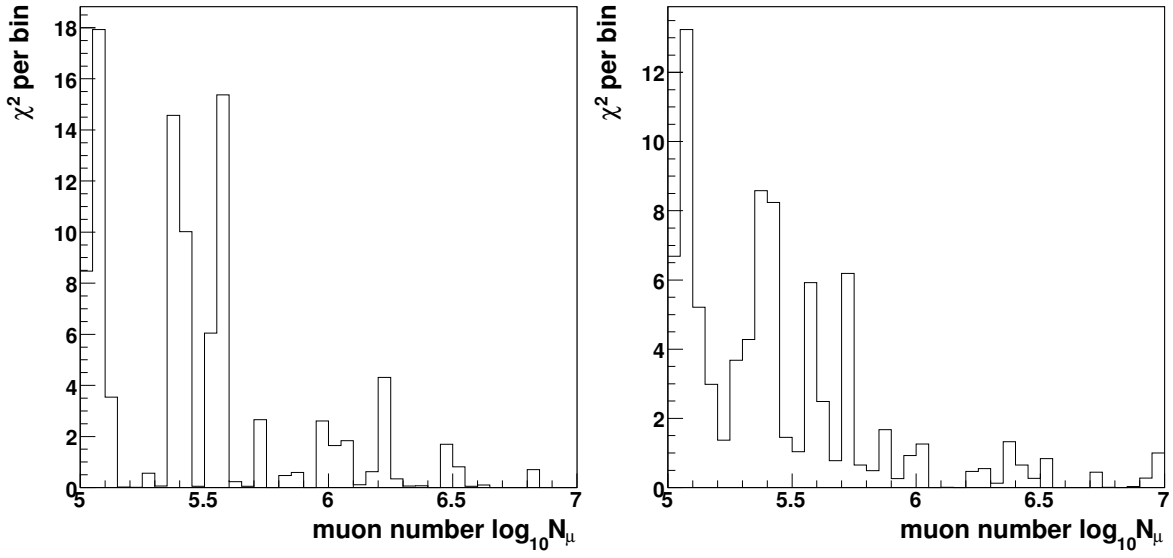

Figure 7.7: Contribution to χ^2 for zenith angles of 0°–18° (left) and 18°–25° (right).

Chapter 8

Conclusion and Outlook

In this work the muon component of extensive air showers measured with the KASCADE-Grande experiment has been investigated.
Reconstruction methods and qualities have been presented, with a focus on the muon component of extensive air showers. It has been shown that, although the radial coverage of the detector is limited, it is possible to reconstruct the muon number with a precision of up to 10%.
The measured muon lateral distributions have been presented. They exhibit in a zenith angle range of 0°–18° a slight steepening for the highest energy interval. For larger zenith angles 18°–25° and 25°–30° this effect weakens.
As expected, due to the limited sensitive area of the KASCADE array, detector resolution, and reconstruction resolution, it is difficult to make a statement concerning a change of composition based on the shape of the measured muon density distribution. A direct comparison of the muon size spectra measured by KASCADE-Grande and KASCADE demonstrates that it is important to know and take into account reconstruction resolutions and systematic effects.
This was achieved by studying the application of unfolding methods to a muon size spectrum with Monte Carlo simulations. As components hydrogen and iron were used to describe the measured muon size spectrum. It was presented that it is possible to reconstruct the total energy spectrum for energies higher than 10^{16} eV, which is the minimum energy that KASCADE-Grande can measure by design.
The analysis of KASCADE-Grande data, taken from March 2004 until March 2006, shows a very good agreement with previous results of KASCADE, which indicates a correct description of the data by the simulations. The reconstructed total energy spectra for zenith angle ranges 0°–18° and 18°–25° extend up to an energy of 3×10^{17} eV. In this range, so far no second knee is seen in the total energy spectrum. Indications of the presence of a knee in this energy region are given by some experiments [2, 15, 41], while other experiments sensitive to the same energy range do not present any similar discontinuity [44]. It is not yet possible for KASCADE-Grande

to exclude the knee nor to confirm it. With more statistics it will be possible with KASCADE-Grande to contribute in solving this puzzle.
The perspective for a study in the interesting energy region is good, since it has been shown in this work that the muon number measured by KASCADE-Grande can be used for unfolding analyses, leading to an energy measurement. The KASCADE-Grande experiment is able to collect in few years a much higher statistic as would it be possible with the KASCADE experiment. Furthermore the upcoming installation of Flash ADC will allow the measurement of the energy deposit in the Grande detectors with a high time resolution, which permits a discrimination between electron and muons with increased radial coverage. In future with higher statistics together with the reconstructed electron number it will be possible to analyze the development of the composition in the cosmic ray energy spectrum at energies higher than 10^{17} eV.

Appendix A

A.1 Response matrices

In the following the elements of the response matrices are listed that were obtained from simulations.
They describe the probabilty that a shower with a given muon number $\log_{10} N_\mu = 4.975 + \mu_i * 0.05$ originates from a primary of energy $\log_{10} E = 5.95 + e_j * 0.1$. Listed are:

- Hydrogen 0°–18°, in Table A.1 and A.2
- Iron 0°–18°, in Table A.3 and A.4
- Hydrogen 18°–25°, in Table A.5 and A.6
- Iron 18°–25°, in Table A.7 and A.8

	e_1	e_2	e_3	e_4	e_5	e_6	e_7	e_8	e_9	e_{10}	e_{11}	e_{12}	e_{13}	e_{14}	e_{15}
μ_1				0.0004	0.0012	0.0021	0.0081	0.031	0.057	0.11	0.14	0.1	0.05	0.018	0.018
μ_2		0.00052		0.0004	0.00083	0.0021	0.004	0.015	0.041	0.071	0.16	0.16	0.076	0.03	0.03
μ_3						0.001	0.0029	0.0051	0.019	0.072	0.12	0.15	0.13	0.073	0.073
μ_4					0.00042	0.00052	0.0012	0.0044	0.011	0.045	0.077	0.13	0.11	0.076	0.076
μ_5							0.00058	0.0022	0.0046	0.024	0.064	0.095	0.15	0.14	0.14
μ_6						0.00052	0.0012	0.00073	0.0018	0.0057	0.033	0.081	0.19	0.15	0.15
μ_7									0.0018	0.0045	0.016	0.047	0.092	0.17	0.17
μ_8										0.0011	0.0026	0.03	0.052	0.11	0.11
μ_9										0.0011	0.0026	0.0016	0.035	0.097	0.097
μ_{10}													0.022	0.067	0.067
μ_{11}											0.0013	0.0047	0.0022	0.036	0.036
μ_{12}														0.0091	0.0091
μ_{13}														0.0061	0.0061
μ_{14}															
μ_{15}															
μ_{16}															
μ_{17}															
μ_{18}															
μ_{19}															
μ_{20}															
μ_{21}															
μ_{22}															
μ_{23}															
μ_{24}															
μ_{25}															
μ_{26}															
μ_{27}															
μ_{28}															
μ_{29}															
μ_{30}															
μ_{31}															
μ_{32}															
μ_{33}															
μ_{34}															
μ_{35}															
μ_{36}															
μ_{37}															
μ_{38}															
μ_{39}															
μ_{40}															

Table A.1: Values of response matrix for hydrogen, 0°–18°.

	e_{16}	e_{17}	e_{18}	e_{19}	e_{20}	e_{21}	e_{22}	e_{23}	e_{24}	e_{25}	e_{26}	e_{27}	e_{28}	e_{29}	e_{30}
μ_1															
μ_2															
μ_3															
μ_4	0.014														
μ_5	0.024	0.0048													
μ_6	0.029	0.014													
μ_7	0.057	0.038		0.01											
μ_8	0.077	0.038	0.011												
μ_9	0.19	0.096	0.017	0.01											
μ_{10}	0.19	0.11	0.04	0.01											
μ_{11}	0.17	0.15	0.13	0.051											
μ_{12}	0.14	0.13	0.19	0.082	0.028										
μ_{13}	0.067	0.18	0.19	0.15	0.046										
μ_{14}	0.024	0.15	0.18	0.22	0.065	0.0099									
μ_{15}	0.019	0.072	0.091	0.21	0.16	0.02									
μ_{16}	0.0048	0.014	0.074	0.16	0.17	0.03	0.011								
μ_{17}			0.034	0.041	0.14	0.11	0.011								
μ_{18}			0.028	0.031	0.19	0.12	0.08		0.021						
μ_{19}			0.011	0.01	0.083	0.26	0.17	0.091	0.043						
μ_{20}			0.0057		0.083	0.25	0.3	0.3	0.043						
μ_{21}			0.0057		0.0093	0.13	0.21	0.061	0.021						
μ_{22}					0.028	0.059	0.14	0.18	0.064						
μ_{23}						0.02	0.057	0.15	0.26	0.12					
μ_{24}							0.023	0.15	0.26	0.24					
μ_{25}								0.061	0.13	0.27					
μ_{26}									0.064	0.15	0.13				
μ_{27}									0.021	0.18	0.087				
μ_{28}									0.021	0.03	0.3				
μ_{29}									0.043		0.087		0.053	0.048	
μ_{30}									0.021		0.3	0.53	0.079	0.19	
μ_{31}											0.087	0.18	0.26	0.048	
μ_{32}												0.18	0.18		
μ_{33}													0.32	0.048	0.12
μ_{34}													0.079		
μ_{35}												0.12		0.38	0.059
μ_{36}													0.026	0.19	0.12
μ_{37}														0.048	0.41
μ_{38}														0.048	0.29
μ_{39}															
μ_{40}															

Table A.2: Continuation of response matrix for hydrogen, 0°–18°.

	e_1	e_2	e_3	e_4	e_5	e_6	e_7	e_8	e_9	e_{10}	e_{11}	e_{12}	e_{13}	e_{14}	e_{15}
μ_1				0.0014	0.0011	0.0099	0.019	0.063	0.13	0.15	0.077	0.025	0.0082		
μ_2					0.0011	0.0033	0.01	0.033	0.1	0.18	0.16	0.048	0.014		
μ_3						0.0022	0.0069	0.018	0.04	0.12	0.19	0.11	0.021		
μ_4							0.0029	0.0087	0.034	0.088	0.19	0.17	0.064	0.0026	0.0026
μ_5							0.00058	0.0036	0.014	0.056	0.15	0.19	0.12	0.023	0.023
μ_6							0.00058		0.0066	0.035	0.081	0.19	0.21	0.072	0.072
μ_7								0.0015	0.00094	0.012	0.052	0.13	0.19	0.13	0.13
μ_8									0.0019	0.0044	0.019	0.064	0.18	0.21	0.21
μ_9										0.0011	0.0062	0.033	0.12	0.23	0.23
μ_{10}											0.0025	0.011	0.045	0.16	0.16
μ_{11}												0.0047	0.0082	0.1	0.1
μ_{12}												0.0047	0.0062	0.039	0.039
μ_{13}														0.021	0.021
μ_{14}														0.01	0.01
μ_{15}														0.0026	0.0026
μ_{16}															
μ_{17}															
μ_{18}															
μ_{19}															
μ_{20}															
μ_{21}															
μ_{22}															
μ_{23}															
μ_{24}															
μ_{25}															
μ_{26}															
μ_{27}															
μ_{28}															
μ_{29}															
μ_{30}															
μ_{31}															
μ_{32}															
μ_{33}															
μ_{34}															
μ_{35}															
μ_{36}															
μ_{37}															
μ_{38}															
μ_{39}															
μ_{40}															

Table A.3: Values of response matrix for iron, 0°–18°.

	e_{16}	e_{17}	e_{18}	e_{19}	e_{20}	e_{21}	e_{22}	e_{23}	e_{24}	e_{25}	e_{26}	e_{27}	e_{28}	e_{29}	e_{30}
μ_1															
μ_2															
μ_3															
μ_4															
μ_5															
μ_6															
μ_7															
μ_8	0.013														
μ_9	0.034														
μ_{10}	0.094														
μ_{11}	0.22	0.019													
μ_{12}	0.26	0.11													
μ_{13}	0.18	0.27	0.041	0.0082											
μ_{14}	0.11	0.3	0.16	0.0082											
μ_{15}	0.068	0.17	0.3	0.12											
μ_{16}	0.017	0.075	0.27	0.12	0.028										
μ_{17}	0.0043	0.042	0.16	0.29	0.11										
μ_{18}		0.0047	0.064	0.28	0.15	0.014									
μ_{19}			0.012	0.15	0.25	0.13									
μ_{20}				0.0082	0.31	0.25									
μ_{21}				0.016	0.14	0.25	0.036								
μ_{22}						0.17	0.2								
μ_{23}						0.17	0.47	0.09							
μ_{24}						0.014	0.29	0.27							
μ_{25}								0.27	0.071						
μ_{26}								0.3	0.39						
μ_{27}								0.075	0.39	0.028					
μ_{28}									0.14	0.31					
μ_{29}										0.56	0.33				
μ_{30}										0.11	0.22	0.026			
μ_{31}											0.33	0.24			
μ_{32}											0.11	0.24	0.071		
μ_{33}												0.34	0.14		
μ_{34}												0.16	0.57	0.12	
μ_{35}													0.14	0.062	
μ_{36}													0.071	0.75	
μ_{37}														0.062	
μ_{38}															0.7
μ_{39}															0.3
μ_{40}															

Table A.4: Continuation of response matrix for iron, 0°–18°.

	e_1	e_2	e_3	e_4	e_5	e_6	e_7	e_8	e_9	e_{10}	e_{11}	e_{12}	e_{13}	e_{14}	e_{15}
μ_1						0.003	0.011	0.013	0.05	0.11	0.13	0.11	0.064	0.024	0.024
μ_2			0.00064		0.00057	0.00059	0.0035	0.0095	0.025	0.06	0.11	0.14	0.084	0.078	0.078
μ_3							0.0035	0.004	0.025	0.032	0.076	0.13	0.12	0.086	0.086
μ_4							0.0014	0.0024	0.01	0.023	0.05	0.1	0.17	0.14	0.14
μ_5								0.00079	0.0031	0.016	0.036	0.073	0.17	0.18	0.18
μ_6							0.0014	0.00079	0.001	0.0091	0.016	0.065	0.11	0.16	0.16
μ_7								0.00079	0.001	0.0013	0.0093	0.044	0.093	0.11	0.11
μ_8									0.0021		0.0016	0.022	0.058	0.089	0.089
μ_9											0.0016	0.014	0.023	0.043	0.043
μ_{10}												0.004	0.012	0.013	0.013
μ_{11}													0.0058	0.016	0.016
μ_{12}															
μ_{13}															
μ_{14}															
μ_{15}															
μ_{16}															
μ_{17}															
μ_{18}															
μ_{19}															
μ_{20}															
μ_{21}															
μ_{22}															
μ_{23}															
μ_{24}															
μ_{25}															
μ_{26}															
μ_{27}															
μ_{28}															
μ_{29}															
μ_{30}															
μ_{31}															
μ_{32}															
μ_{33}															
μ_{34}															
μ_{35}															
μ_{36}															
μ_{37}															
μ_{38}															
μ_{39}															
μ_{40}															

Table A.5: Values of response matrix for hydrogen, 18°–25°.

	e_{16}	e_{17}	e_{18}	e_{19}	e_{20}	e_{21}	e_{22}	e_{23}	e_{24}	e_{25}	e_{26}	e_{27}	e_{28}	e_{29}	e_{30}
μ_1															
μ_2	0.0061														
μ_3	0.018		0.0078												
μ_4	0.0061		0.0078												
μ_5	0.036	0.0071													
μ_6	0.12		0.0078												
μ_7	0.067	0.043	0.0078												
μ_8	0.15	0.021	0.016												
μ_9	0.16	0.085	0.023												
μ_{10}	0.15	0.13	0.023	0.041											
μ_{11}	0.13	0.21	0.093	0.092	0.021										
μ_{12}	0.079	0.18	0.14	0.1											
μ_{13}	0.061	0.17	0.17	0.1	0.031										
μ_{14}	0.012	0.11	0.17	0.24	0.1	0.017									
μ_{15}		0.035	0.16	0.17	0.14	0.086	0.028								
μ_{16}			0.12	0.12	0.22	0.069	0.028								
μ_{17}		0.0071	0.054	0.061	0.33	0.26	0.083								
μ_{18}			0.0078	0.031	0.12	0.28	0.083								
μ_{19}				0.031	0.01	0.14	0.14	0.12							
μ_{20}					0.01	0.1	0.28	0.042							
μ_{21}					0.01		0.17	0.12		0.016					
μ_{22}						0.052	0.14	0.33	0.031	0.033					
μ_{23}							0.056	0.17	0.12	0.049	0.065				
μ_{24}								0.17	0.12	0.11					
μ_{25}								0.042	0.38	0.13	0.065				
μ_{26}									0.25	0.26	0.19				
μ_{27}									0.094	0.2	0.19				
μ_{28}										0.18	0.23				
μ_{29}										0.016	0.16	0.42			
μ_{30}											0.097	0.5			
μ_{31}												0.083			
μ_{32}														0.38	
μ_{33}													1	0.38	0.11
μ_{34}														0.077	0.22
μ_{35}														0.15	0.22
μ_{36}															0.44
μ_{37}															
μ_{38}															
μ_{39}															
μ_{40}															

Table A.6: Continuation of response matrix for hydrogen, 18°–25°.

	e_1	e_2	e_3	e_4	e_5	e_6	e_7	e_8	e_9	e_{10}	e_{11}	e_{12}	e_{13}	e_{14}	e_{15}
μ_1					0.00097	0.0017	0.018	0.049	0.097	0.19	0.13	0.031	0.014		
μ_2					0.00097	0.0025	0.005	0.02	0.059	0.14	0.17	0.078	0.034		
μ_3							0.0067	0.013	0.033	0.12	0.18	0.13	0.045	0.0073	0.0073
μ_4							0.00083	0.0061	0.016	0.058	0.13	0.24	0.11	0.0073	0.0073
μ_5									0.0079	0.034	0.1	0.19	0.13	0.055	0.055
μ_6								0.001	0.0034	0.012	0.057	0.15	0.21	0.088	0.088
μ_7										0.0082	0.028	0.087	0.17	0.22	0.22
μ_8											0.015	0.037	0.15	0.21	0.21
μ_9											0.0016	0.017	0.081	0.18	0.18
μ_{10}							0.00083				0.0016	0.0044	0.028	0.15	0.15
μ_{11}										0.0014			0.014	0.051	0.051
μ_{12}										0.0014			0.0056	0.018	0.018
μ_{13}														0.011	0.011
μ_{14}															
μ_{15}															
μ_{16}															
μ_{17}															
μ_{18}															
μ_{19}															
μ_{20}															
μ_{21}															
μ_{22}															
μ_{23}															
μ_{24}															
μ_{25}															
μ_{26}															
μ_{27}															
μ_{28}															
μ_{29}															
μ_{30}															
μ_{31}															
μ_{32}															
μ_{33}															
μ_{34}															
μ_{35}															
μ_{36}															
μ_{37}															
μ_{38}															
μ_{39}															
μ_{40}															

Table A.7: Values of response matrix for iron, 18°–25°.

	e_{16}	e_{17}	e_{18}	e_{19}	e_{20}	e_{21}	e_{22}	e_{23}	e_{24}	e_{25}	e_{26}	e_{27}	e_{28}	e_{29}	e_{30}
μ_1															
μ_2															
μ_3															
μ_4															
μ_5															
μ_6															
μ_7	0.0045														
μ_8	0.0089														
μ_9	0.098	0.0057													
μ_{10}	0.16	0.011													
μ_{11}	0.19	0.086													
μ_{12}	0.25	0.16	0.034												
μ_{13}	0.16	0.3	0.095												
μ_{14}	0.085	0.19	0.23	0.051											
μ_{15}	0.022	0.18	0.33	0.18	0.012										
μ_{16}	0.018	0.057	0.19	0.29	0.037										
μ_{17}	0.0045	0.0057	0.11	0.16	0.16										
μ_{18}		0.0057		0.19	0.32	0.019									
μ_{19}			0.0086	0.11	0.32	0.11									
μ_{20}				0.01	0.099	0.54									
μ_{21}					0.037	0.28	0.31								
μ_{22}					0.012	0.056	0.31	0.094							
μ_{23}							0.31	0.19							
μ_{24}							0.083	0.44	0.04						
μ_{25}								0.25	0.28						
μ_{26}								0.031	0.36	0.097					
μ_{27}									0.32	0.19					
μ_{28}										0.42					
μ_{29}										0.29	0.25				
μ_{30}											0.38				
μ_{31}											0.25	0.14			
μ_{32}											0.12	0.57	0.21	0.12	
μ_{33}												0.29	0.37		
μ_{34}													0.42	0.059	0.1
μ_{35}														0.18	
μ_{36}														0.47	0.1
μ_{37}														0.18	0.5
μ_{38}															0.3
μ_{39}															
μ_{40}															

Table A.8: Continuation of response matrix for iron, 18°–25°.

A.2 WMSE for simulation sets

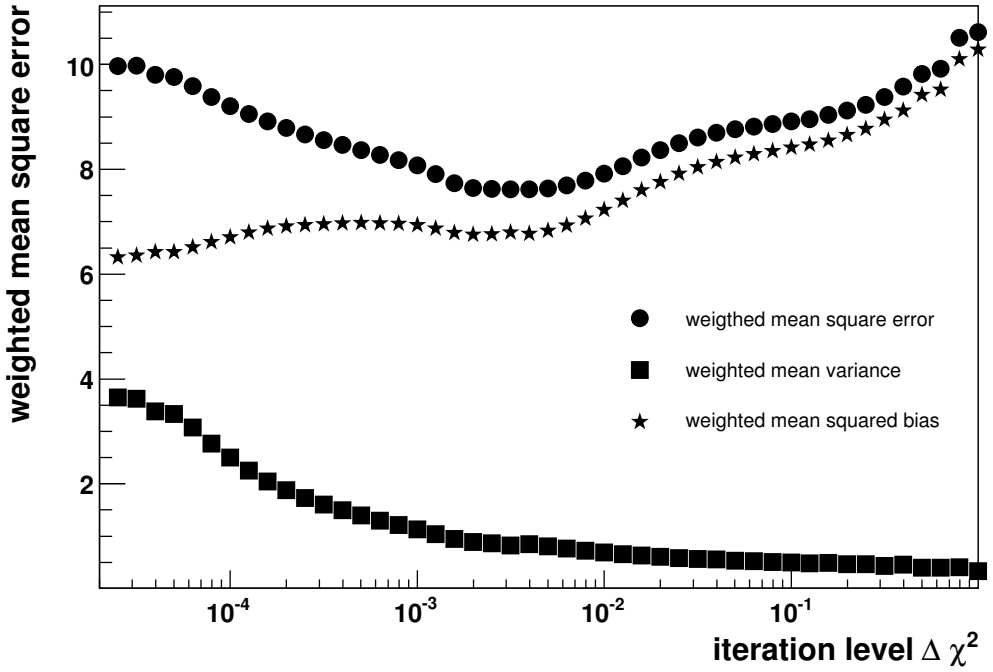

Figure A.1: Total weighted mean square error depending on iteration quality $\Delta\chi^2$ for set 2.

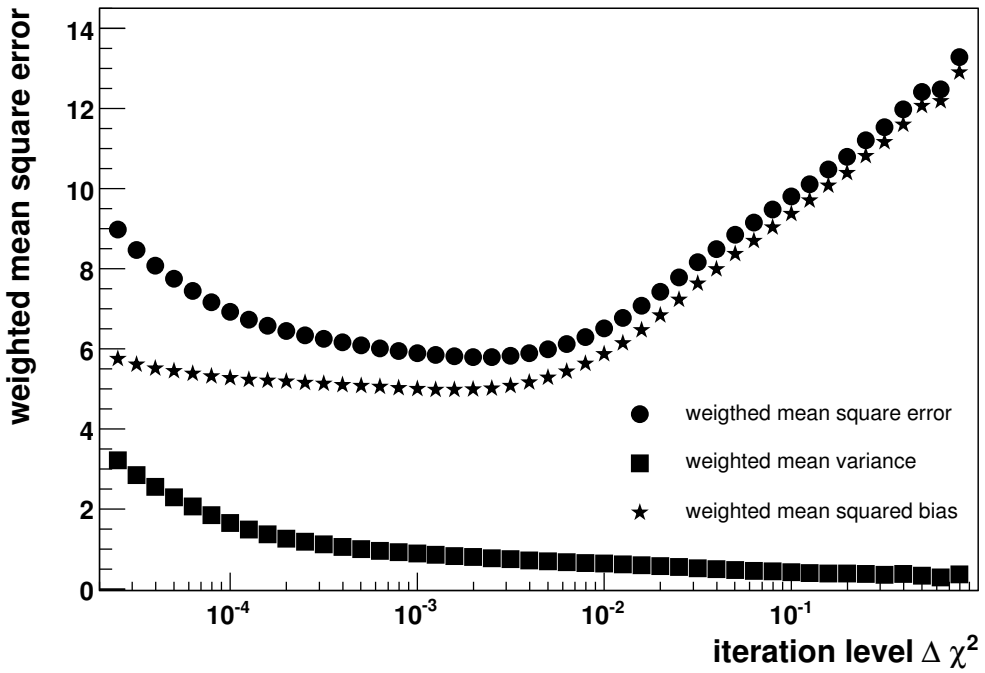

Figure A.2: Total weighted mean square error depending on iteration quality $\Delta\chi^2$ for set 3.

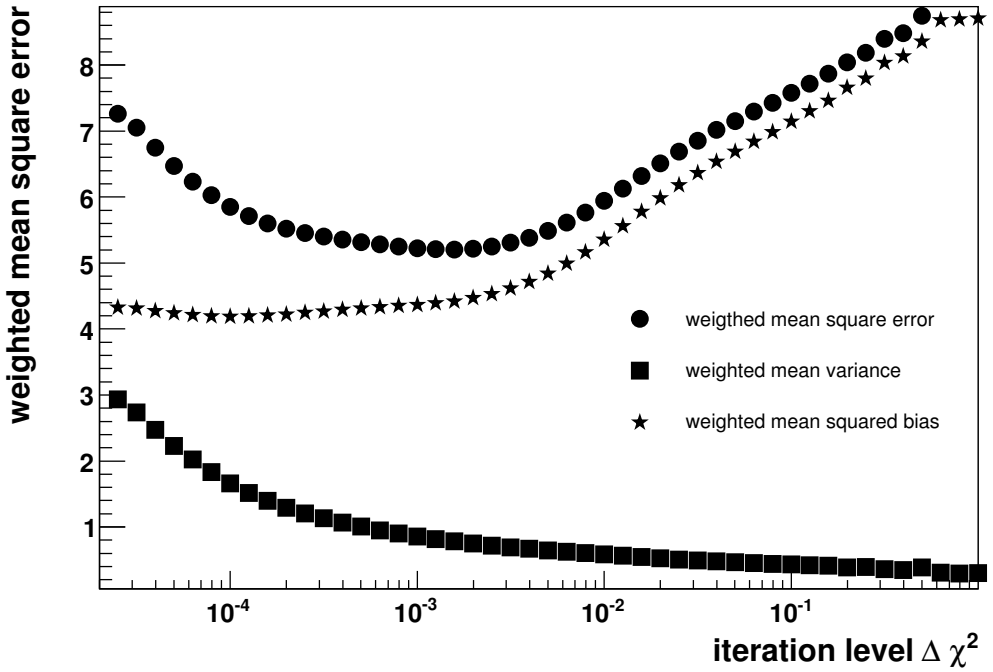

Figure A.3: Total weighted mean square error depending on iteration quality $\Delta\chi^2$ for set 4.

Bibliography

[1] R. U. Abbasi et al. A study of the composition of ultra high energy cosmic rays using the High Resolution Fly's Eye. *Astrophys. J.*, 622:910–926, 2005.

[2] T. Abu-Zayyad et al. Measurement of the cosmic ray energy spectrum and composition from 10^{17} eV to $10^{18.3}$ eV using a hybrid fluorescence technique. *Astrophys. J.*, 557:686–699, 2001.

[3] M. Aglietta et al. The EAS TOP Array at E(0) = 10^{14} eV - 10^{16} eV: Stability and Resolutions. *Nucl. Instrum. Meth.*, A277:23–28, 1989.

[4] M. Aglietta et al. UHE cosmic ray event reconstruction by the electromagnet detector of EAS-TOP. *Nucl. Instrum. Meth.*, A336:310–321, 1993.

[5] F. A. Aharonian et al. High-energy particle acceleration in the shell of a supernova remnant. *Nature*, 432:75–77, 2004.

[6] Carl D. Anderson. Cosmic-Ray Positive and Negative Electrons. *Physical Review*, 44:406–416, September 1933.

[7] Carl D. Anderson and Seth H. Neddermeyer. Nature of Cosmic-Ray Particles. *Review of Modern Physics*, 11, July 1939.

[8] T. Antoni. Measurement of high energy muons in extended air showers at KASCADE. (In German). Forschungszentrum Karlsruhe, FZKA-6903.

[9] T. Antoni et al. Electron, muon, and hadron lateral distributions measured in air-showers by the KASCADE experiment. *Astropart. Phys.*, 14:245–260, 2001.

[10] T. Antoni et al. The Cosmic ray experiment KASCADE. *Nucl. Instrum. Meth.*, A513:490–510, 2003.

[11] T. Antoni et al. KASCADE measurements of energy spectra for elemental groups of cosmic rays: Results and open problems. *Astropart. Phys.*, 24:1–25, 2005.

[12] W. D. Apel et al. Comparison of measured and simulated lateral distributions for electrons and muons with KASCADE. *Astropart. Phys.*, 24:467–483, 2006.

[13] P. Auger, P. Ehrenfest, R. Maze, J. Daudin, and R. A. Fréon. Extensive Cosmic-Ray Showers. *Reviews of Modern Physics*, 11:288–291, July 1939.

[14] John N. Bahcall and Eli Waxman. Has the GZK cutoff been discovered? *Phys. Lett.*, B556:1–6, 2003.

[15] D. J. Bird et al. The Cosmic ray energy spectrum observed by the Fly's Eye. *Astrophys. J.*, 424:491–502, 1994.

[16] D. J. Bird et al. Detection of a cosmic ray with measured energy well beyond the expected spectral cutoff due to cosmic microwave radiation. *Astrophys. J.*, 441:144–150, 1995.

[17] H. Bozdog et al. The detector system for measurement of multiple cosmic muons in the central detector of KASCADE. *Nucl. Instrum. Meth.*, A465:455–471, 2001.

[18] R. Brun and F. Carminati. GEANT- Detector Description and Simulation Tool. *CERN Program Library Long Writeup*, 1993.

[19] Julian Candia, Esteban Roulet, and Luis N. Epele. Turbulent diffusion and drift in galactic magnetic fields and the explanation of the knee in the cosmic ray spectrum. *JHEP*, 12:033, 2002.

[20] K. S. Cheng, C. Ho, and M. Ruderman. Energetic radiation from rapidly spinning pulsars. I - Outer magnetosphere gaps. II - VELA and Crab. *Astrophys. J.*, 300:500–539, 1986.

[21] P. Doll et al. Muon tracking detector for the air shower experiment KASCADE. *Nucl. Instrum. Meth.*, A488:517–535, 2002.

[22] L O'C Drury. An introduction to the theory of diffusive shock acceleration of energetic particles in tenuous plasmas. *Reports on Progress in Physics*, 46(8):973–1027, 1983.

[23] J. Engler et al. A warm-liquid calorimeter for cosmic-ray hadrons. *Nucl. Instrum. Meth.*, A427:528–542, 1999.

[24] R. Enomoto et al. The Acceleration of cosmic ray protons in the supernova remnant RX J1713.7-3946. *Nature*, 416:823–826, 2002.

[25] A. D. Erlykin and A. W. Wolfendale. A single source of cosmic rays in the range 10^{15} eV to 10^{16} eV. *J. Phys.*, G23:979–989, 1997.

[26] A. Fasso, A. Ferrari, P. R. Sala, and J. Ranft. FLUKA: Status and prospective for hadronic applications. Prepared for International Conference on Advanced Monte Carlo for Radiation Physics, Particle Transport Simulation and Applications (MC 2000), Lisbon, Portugal, 23-26 Oct 2000.

[27] E. Fermi. On the Origin of the Cosmic Radiation. *Physical Review*, 75, 1949.

[28] R. Glasstetter et al. Shower Reconstruction Performance of KASCADE-Grande. *Forschungszentrum Karlsruhe, FZKA-6890*, 2003. Prepared for 28th International Cosmic Ray Conferences (ICRC 2003), Tsukuba, Japan, 31 Jul - 7 Aug 2003, Vol 2, 781.

[29] R. Glasstetter et al. Shower Size Reconstruction at KASCADE-Grande. *Forschungszentrum Karlsruhe, FZKA-7187*, 2005. Prepared for 29th International Cosmic Ray Conferences (ICRC 2005), Poona, India, 3 - 10 Aug 2005.

[30] R. Gold. An iterative unfolding method for matrices. *Argonne National Laboratory*, ANL-6984, 1964.

[31] K. Greisen. The Extensive Air Showers. *Progess in Elementary Particle and Cosmic Ray Physics*, 3, 1956.

[32] Kenneth Greisen. End to the cosmic ray spectrum? *Phys. Rev. Lett.*, 16:748–750, 1966.

[33] A.K. Harding and T.K. Gaisser. Acceleration by pulsar winds in binary systems. *Astrophys. J.*, 358:561–574, 1990.

[34] D. Heck, G. Schatz, T. Thouw, J. Knapp, and J. N. Capdevielle. CORSIKA: A Monte Carlo code to simulate extensive air showers. *Forschungszentrum Karlsruhe, FZKA-6019*, 1998.

[35] V. Hess. Über Beobachtungen der durchdringenden Strahlung bei sieben Freiballonfahrten. *Physikalische Zeitschrift*, 13:1084–1091, 1912.

[36] J. R. Jokipii and G. Morfill. Ultra-high-energy cosmic rays in a galactic wind and its termination shock. *Astrophys. J.*, 312:170–177, 1987.

[37] N. N. Kalmykov and S. S. Ostapchenko. The Nucleus-nucleus interaction, nuclear fragmentation, and fluctuations of extensive air showers. *Phys. Atom. Nucl.*, 56:346–353, 1993.

[38] K. Kamata and J. Nishimura. The Lateral and the Angular Structure Functions of Electron Showers. *Prog. Theoret. Phys. Suppl*, 6, 1958.

[39] D. Kazanas and A. Nicolaidis. Cosmic rays and large extra dimensions. *Gen. Rel. Grav.*, 35:1117–1123, 2003.

[40] G. Kulikov and G. Kristiansen. *Journal of Experimental and Theoretical Physics*, 35, 1958.

[41] S.P. Kurenko et al. Characteristics of EAS and Primary Particle Mass Composition in the Energy Region of 10^{17} – 10^{19} eV by Yakutsk Data. 2004.

[42] P. O. Lagage and C. J. Cesarsky. The maximum energy of cosmic rays accelerated by supernova shocks. *Astron. Astrophys.*, 125:249–257, 1983.

[43] A. A. Lagutin and R. I. Raikin. Lateral distribution of electrons in EAS at superhigh energies: predictions and experimental data. *Nucl. Phys. Proc. Suppl.*, 97:274–277, 2001.

[44] M. Nagano et al. Energy spectrum of primary cosmic rays above 10^{17} eV determined from the extensive air shower experiment at Akeno. *J. Phys.*, G18:423–442, 1992.

[45] W. Ralph Nelson, H. Hirayama, and David W. O. Rogers. The EGS4 Code Ssystem. *SLAC-0265*, Stanford Linear Accelerator Center, 1985.

[46] S. I. Nikolsky. Break in the cosmic ray spectrum or confinement violation near 10^6 TeV? *Nucl. Phys. Proc. Suppl.*, 39A:228–234, 1995.

[47] D.L. Phillips. A technique for the numerical solution of certain integrals of the first kind. *J. ACM*, 9:84, 1962.

[48] V. S. Ptuskin, S. I. Rogovaya, V. N. Zirakashvili, L. G. Chuvilgin, G. B. Khristiansen, E. G. Klepach, and G. V. Kulikov. Diffusion and drift of very high energy cosmic rays in galactic magnetic fields. *Astron. Astrophys.*, 268:726–735, February 1993.

[49] Jorg P. Rachen and Peter L. Biermann. Extragalactic ultrahigh-energy cosmic rays. 1. Contribution from hot spots in FR-II radio galaxies. *Astron. Astrophys.*, 272:161–175, 1993.

[50] U. Raidt. Setup of the trigger and timing facility of the KASCADE central detector and investigation of muon arrival times in extended air showers. (In German). FZKA-5917.

[51] C.E. Shannon. A mathematical theory of communication. *Bell. Sys. Tech. J.*, 27:379, 1948.

[52] Guenter Sigl. The enigma of the highest energy particles of nature. *Ann. Phys.*, 303:117–141, 2003.

[53] R. W. Springer. Measurement of the flux of UHE cosmic rays by the HiRes detectors observing in both monocular and stereoscopic modes. Prepared for 28th International Cosmic Ray Conferences (ICRC 2003), Tsukuba, Japan, 31 Jul - 7 Aug 2003.

[54] M. Takeda et al. Extension of the cosmic-ray energy spectrum beyond the predicted Greisen-Zatsepin-Kuzmin cutoff. *Phys. Rev. Lett.*, 81:1163–1166, 1998.

[55] Masahiro Takeda et al. Energy determination in the Akeno Giant Air Shower Array experiment. *Astropart. Phys.*, 19:447–462, 2003.

[56] A.N. Tikhonov. On the solution of improperly posed problems and the method of regularization . *Sov. Math.*, 5:1035, 1963.

[57] Holger Ulrich. Untersuchungen zum primären Energiespektrum der kosmischen Strahlung im PeV-Bereich mit dem KASCADE-Experiment. *Forschungszentrum Karlsruhe, Wiss. Ber. FZKA*, 6952, 2004.

[58] P. H. van Cittert. Zum Einfluß der Spaltbreite auf die Intensitätsverteilung in Spektrallinien. II. *Zeitschrift für Physik*, 69:298, 1931.

[59] Richard Wigmans. On big bang relics, the neutrino mass and the spectrum of cosmic rays. *Nucl. Phys. Proc. Suppl.*, 85:305–310, 2000.

[60] G. T. Zatsepin and V. A. Kuzmin. Upper limit of the spectrum of cosmic rays. *JETP Lett.*, 4:78–80, 1966.